Proceedings of the
Annual Stability Conference
Structural Stability Research Council
Louisville, Kentucky, April 13-16, 2021

Post-buckling behavior of thin-walled regular polygonal tubes subjected to bending

André D. Martins[1], Rodrigo Gonçalves[2], Dinar Camotim[3]

Abstract

This work presents and discusses numerical results concerning the elastic post-buckling behavior and imperfection sensitivity of regular convex polygonal cross-section (RCPS) tubular beams buckling in local, distortional and mixed local-distortional modes, a topic currently lacking research. This study is carried out in the framework of Generalized Beam Theory (GBT) geometrically non-linear analyses, enriched with a branch switching technique, and takes advantage of the GBT intrinsic modal nature to shed new light on the mechanics underlying the post-buckling behavior of these members. Due to the small half-wavelength of all the buckling phenomena addressed, only simply supported members under uniform bending are investigated. In particular, this work investigates the post-buckling behavior and imperfection sensitivity of RCPS beams (i) exhibiting several wall numbers (6, 8, 10, 14, 20, 30) with distinct combinations of circumradius-to-thickness ratios (ii) having distinct lengths, and (iii) containing critical-mode initial geometrical imperfections with several amplitudes. Relevant displacement profiles and modal participation diagrams are provided along trivial and non-trivial equilibrium paths, in order to draw meaningful conclusions concerning the post-buckling behavior of RCPS tubes under bending. For comparison and validation purposes, ABAQUS shell finite element results are also presented.

1. Introduction

Thin-walled tubes with regular convex polygonal cross-sections (RCPS) are widely used in the construction industry (*e.g.*, in communication towers, posts supporting lighting equipment or overhead power lines) and can also be used as an alternative to circular hollow section members. However, the current knowledge on the behavior of RCPS members is fairly limited, as attested by the reduced number of publications available in prestigious international journals – the experimental work by Bulson (1969) is a rare example. Recently, the authors investigated the buckling behavior of RCPS members under uniform compression (Gonçalves & Camotim 2013a) and bending or torsion (Gonçalves & Camotim 2013b), using a special Generalized Beam Theory (GBT) formulation (Gonçalves & Camotim 2013c) that accounts for the RCPS rotational symmetry. These studies unveiled several peculiar behavioral features, such as (i) columns are susceptible to cross-section distortion and exhibit duplicate local and distortional bucking modes, and (ii) beams with small (large) wall numbers combined with small (large) circumradius-to-thickness ratios are susceptible to distortional (local) buckling. More

---

[1] Postdoctoral Researcher, Instituto Superior Técnico, University of Lisbon, <andrerdmartins@tecnico.ulisboa.pt>
[2] Associate Professor, Faculdade de Ciências e Tecnologia, Universidade Nova de Lisboa, <rodrigo.goncalves@fct.unl.pt>
[3] Professor, Instituto Superior Técnico, University of Lisbon, <dcamotim@civil.ist.utl.pt>

recently, the research conducted on columns was extended to the local, distortional (Martins *et al.* 2019a) and local-distortional interactive (Martins *et al.* 2019b) post-buckling behaviors, and it was found that the (i) local post-buckling response is highly stable and unaffected by the duplicate buckling modes, whereas (ii) its distortional counterpart is slightly unstable and exhibits secondary equilibrium paths along the descending branch. Therefore, this investigation aims at continuing the research carried out in the past couple of years, by studying the post-buckling behavior of RCPS subjected to bending – simultaneously a topic lacking research and a type of loading commonly encountered in practice. In other words, the work presented here extends the research reported by Gonçalves & Camotim (2013b) to the post-buckling range, using GBT analyses (*e.g.*, Schardt 1898, Camotim *et al.* 2010a,b and Camotim & Basaglia 2013).

Before addressing the outline of the paper and since the available studies on bent RCPS tubes are fairly scarce, a brief state-of-art literature review on circular tubes subjected to bending is presented next – it includes some classical publications. Almost 100 years ago, Brazier (1927) examined a long thin circular tube (toroidal shell) subjected to bending and showed that there is a gradual non-linear stiffness reduction that leads to a maximum/failure bending moment (limit point). Both the longitudinal compression and tension have components pointing towards the neutral axis, which tend to flatten the circular tube into a quasi-oval shape, a behavioral feature nowadays widely known as *Brazier effect*[4] – the above work also provides an approximation for the maximum bending moment, *i.e.*, the *Brazier moment.* This non-linear behavior was confirmed experimentally in the context of long thin tubular beams made of celluloid. Several authors have subsequently examined this phenomenon, which may trigger localized deformation in the compression side, leading to a sudden collapse occurring even in the material linear elastic range. Reissner & Weinitschke (1963) provided an approximate solution for the non-linear differential equations governing the instability of cylindrical tubes under pure bending, consisting of (i) a power expansion of a dimensionless parameter and (ii) an iterative solution of a system of two simultaneously non-linear integral equations. Kyriakides & Ju (1992) conducted an experimental test campaign involving eleven aluminum 6061-T6 cylindrical tubes exhibiting (i) diameter-to-thickness ratios comprised between 19.5 and 60.5, and (ii) length-to-diameter ratios varying between 18 and 30 – it was found that the former ratio plays a key role in the tube structural response. In a twin paper (Ju & Kyriakides 1992), the authors investigated numerically the buckling and post-buckling behavior of the same aluminum 6061-T6 cylindrical tubes (several diameter-to-thickness ratios), adopting Sander's non-linear shell equations (Sander 1963). Wierzbicki & Sinmao (1997) formulated a simplified theoretical model for cylindrical tubes made of perfectly plastic and strain-hardening materials subjected to pure bending, which is valid for large sectional distortion – for a particular case, the results provided by this model were compared with those appearing in the ABAQUS Example Manual (Section 4.2.1 – version 4-6). Tatting *et al.* (1997) derived and solved, by means of finite differences, governing equations to investigate the (non-linear) bending response of composite circular tubes – these equations are based on classical non-linear shell theory with semi-membrane constitutive assumptions. The results were restricted to compressive stresses below those yielded by the Seide & Weingarden formula, corresponding to the onset of local buckling. The authors (i) provided general solutions for several non-dimensional length and shear length parameters, (ii) studied the influence of the end boundary conditions and (iii) compared their results with those reported by other authors. Wadee *et al.* (2006) derived a variational model based on combining Reissner's model (Reissner 1961) with Timoshenko beam theory and aimed at investigating the localization of deformation ("kinks") in thin-walled elastic circular tubes under pure bending – the system of ODE's was

---

[4] Naturally, this inherent geometrically non-linear effect also occurs in open-section beams – a phenomenon usually denoted *flange-curling* (*e.g.*, Bernard *et al.* (1996), Lecce & Rasmussen (2008), Martins *et al.* (2018a)), characterized by the fact that the flanges tend to move towards the neutral axis (particularly relevant effect in wide flanges).

solved for three distinct cases. Kim *et al.* (2016) developed a simple analytical model, consisting of a modified Brazier approach, to predict the ultimate strength of stiffened circular composite spars subjected to bending. This model was compared with (i) shell finite element models employing several laminate layups/configurations and two bending arrangements (cantilever and four-point bending), and (ii) one (static) experimental test – there was good agreement in both cases. More recently, Yadav & Gerasimidis (2019) investigated numerically (ABAQUS shell finite element analyses – SFEA) the elastic-plastic post-buckling behavior and imperfection sensitivity of purely bent cylindrical shells with radius-to-thickness ratios comprised between 60 and 120. Special attention was devoted to assessing the influence of distinct (i) geometrical imperfection shapes (critical-mode shape, dimple-like imperfection and axisymmetric harmonic imperfection with longitudinally constant or varying amplitude), and (ii) strain-hardening models (parameters of the adopted Ramberg-Osgood stress-strain curves). It was found that the cylindrical shells are highly sensitive to imperfections and that the strain-hardening model also plays an important role in their structural response.

This work presents and discusses numerical results, obtained by means of geometrically non-linear GBT analyses (Martins *et al.* 2018b, Gonçalves & Camotim 2012) enriched with a branch switching technique, concerning the elastic buckling and post-buckling behavior and imperfection sensitivity of RCPS beams buckling in local, distortional and mixed local-distortional modes. Due to the small half-wavelength of the buckling phenomena involved, only simply supported members under uniform bending are considered – recall that non-uniform bending and end boundary condition effects have little relevance. In particular, taking advantage of the GBT modal nature, new light is shed on the mechanics underlying the post-buckling behavior and strength of these members. The outline of the paper is as follows. Section 2 addresses the buckling (bifurcation) behavior of RCPS beams, (i) revisiting and enhancing the work carried out by Gonçalves & Camotim (2013b) and (ii) justifying the geometry selection of the beams analyzed in Section 3. Then, Section 3 (the main section) presents and discusses results concerning the elastic post-buckling behaviors of RCPS beams buckling in local (Section 3.1), distortional (Section 3.2) and mixed local-distortional (Section 3.3) modes. These results are obtained through GBT geometrically non-linear analyses and validated by means of the comparison with values yielded by refined ABAQUS shell finite element models (Simulia Inc 2009). Lastly, Section 4 highlights the most relevant findings of this work and identifies key issues on this topic/field that need to be investigated in the near future.

2. Buckling (Bifurcation) Behavior and Beam Geometry Selection

2.1 Buckling behavior

RCPS members subjected to bending either buckle in local (null displacements of the wall ends and null warping), distortional (non-null displacements of the wall ends and warping) or mixed local-distortional (combining local and distortional features) modes. In fact, depending on the circumradius-to-thickness ratio β_2, a given polygonal tubular beam with n walls may buckle in either of the above three types of modes. In order to illustrate this assertion, Fig. 1, which constitutes an enhanced version of a similar figure appearing in Gonçalves & Camotim (2013b), (i) plots the minimum buckling coefficient k (determined using the program GBTUL, developed by Bebiano *et al.* 2018) versus β_2 for $10 \leq \beta_2 \leq 200$, $n=\{6,7,8,10,12,14,17,20,23,25,28,30,33,35\}$ and r=100mm, (ii) several representative buckling mode shapes, for $n=\{6,8,10,14,20,28,35\}$ and $\beta_2=\{10,20,50,100,150,200\}$, and (iii) the buckling coefficient k_c, corresponding to the axisymmetric buckling of circular tubes under uniform compression[5], since it was shown that it provides good estimates of the local buckling stresses of circular tubes under

---

[5] k_c is obtained by replacing, in Eq. (2), σ_{cr} in Eq. (2) with $\sigma_{cr.c}$ (given by Eq. (3)).

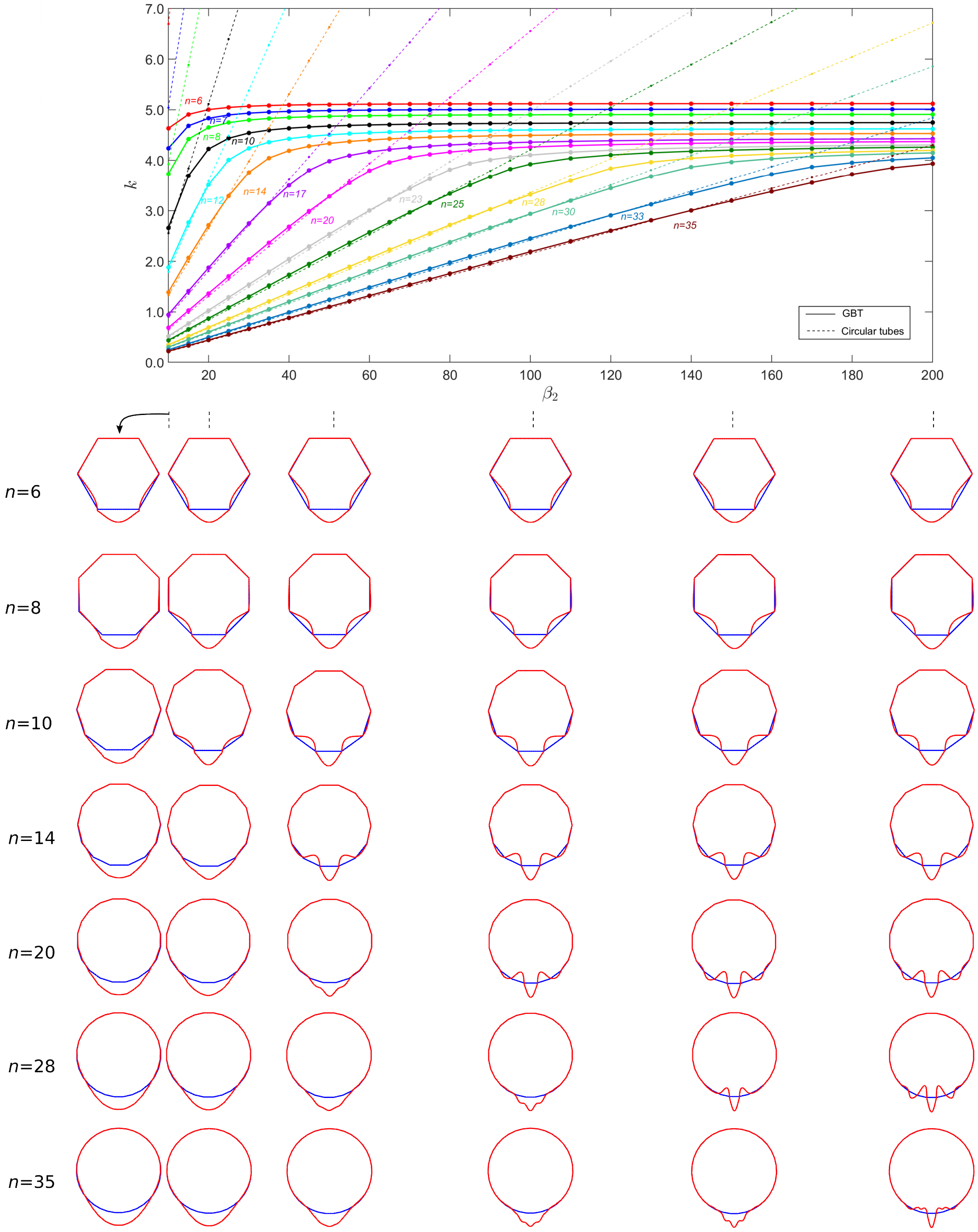

Figure 1: Buckling coefficients and critical buckling modes of uniformly bent RCPS members (θ=0º and r=100mm).

bending ($\sigma_{cr.c}$) (Timoshenko & Gere 1961) (dashed curves in Fig. 1) – note that all the results presented concern simply supported beams under a uniform bending moment compressing uniformly the bottom wall[6] (θ=0º, using the nomenclature adopted by Gonçalves & Camotim 2013b) and that the values of β_2, k and $\sigma_{cr.c}$ are given by

$$\beta_2 = \frac{r}{t} \tag{1}$$

$$k = \frac{48(1-\nu^2)\beta_2^2 \sin^2(\pi / n)\sigma_{cr}}{E\pi^2} \tag{2}$$

$$\sigma_{cr.c} = \frac{E}{\beta_2 \sqrt{3(1-\nu^2)}} \tag{3}$$

where r is the circumradius, t is the wall thickness, ν is Poisson's ratio, E is Young's modulus and σ_{cr} is the critical stress. Note that k is derived from the classical plate buckling formula

$$\sigma_{cr} = k \frac{\pi^2 E}{12(1-\nu^2)} \left(\frac{t}{b}\right)^2 \tag{4}$$

with the wall width equal to $b=2r\sin(\pi/n)$. E=210MPa and ν=0.3 are adopted in this work. The analysis of the results presented in Fig. 1 makes it possible to conclude that:

(i) For a given wall number n, k increases with β_2 until a plateau is reached, corresponding to beams buckling in pure local modes (no corner displacements). This plateau is reached for increasingly larger β_2 values as n grows – note that, for n=35, the plateau is attained for β_2>200. Thus, the RCPS beam and cylindrical tube behaviors potentially differ, even for very large n values – in theory, there is always a minimum β_2 value after which the RCPS beams buckle in *local-plate* modes.

(ii) For $k \cong k_c$, (*i.e.*, k close to the dashed lines in Fig. 1) and n>10, it is observed that the beams buckle in distortional modes. As previously reported by several authors (*e.g.*, Silvestre 2007), in the context of circular tubes, the analytical formula (3), regarding axisymmetric buckling under uniform compression, provides quite good critical stress estimates for tubes under uniform bending. This is also the case for RCPS beams buckling in distortional modes (Gonçalves & Camotim 2013b).

(iii) Taking into account the contents of the previous items and the β_2 range considered ($10 \leq \beta_2 \leq 200$), it is concluded that, for n<10, the beams buckle either (iii$_1$) in mixed local-distortional modes (low β_2 values – *e.g.*, see the buckling modes of beams n=6+β_2=10, n=8+β_2=20 or n=10+β_2=20, clearly showing non-negligible displacements of the most compressed corners) or (iii$_2$) in local modes. For $n \geq 10$, on the other hand, the RCPS beams may buckle in either distortional, mixed local-distortional or local modes.

In order to provide a better insight on the parameter ranges associated with the occurrence of the three buckling phenomena under consideration, the participations of all local (p_L) and distortional (p_D) GBT deformation modes in the beam buckling modes were determined for all the n and β_2 values considered (14×29 cases). Since the local (distortional) buckling mode shapes contain either null or negligible contributions from distortional (local) deformation modes, the ratio η, defined as

$$\eta = \frac{p_L}{p_L + p_D} \tag{5}$$

---

[6] This means that, both for odd or even wall numbers, the cross-section is rotated such that its bottom wall is horizontal, which means that a horizontal applied moment causes uniform compression at that wall.

is able to provide the sought insight. The values $\eta\approx1.0$ and $\eta\approx0.0$ concern beams buckling in pure local and distortional modes, respectively – note that η can also be viewed as quantifying the amount of displacement-restraint at the RCPS corners, varying between 0.0 (no restraint) and 1.0 (full restraint). Fig. 2(a) shows the variation of η with n and β_2, and was obtained using the MATLAB surface-fitting features (based on the thin-plate spline technique – all data with the same "weight") – the η values concerning the beams with the 406 cross-section geometries considered correspond to the dots in Fig. 2(a). An alternative 2D representation of the results is displayed in Fig. 2(b): η-isocurves (curves providing the variation of β_2 with n for a given η). These figures show/confirm the existence of two clearly distinct regions ($\eta\approx1.0$ and $\eta\approx0.0$ – red and blue regions in Fig. 2(a), respectively) and the presence of two plateaus, connected by a rather steep transition surface curve. As discussed in Section 3.3, the η value is strongly related to the beam post-buckling behavior. Fig. 2(b) also shows that the η-isocurves (i) are roughly parallel for $0.1<\eta<0.80$ (range concerning the above steep transition surface), and (ii) exhibit plateaus for $\eta<0.10$ and $\eta\geq0.80$ – the former has virtually null values (pure distortional buckling). Fig. 2(b) still displays a curve corresponding to equal values of the buckling coefficients associated with the (i) critical buckling (k – expression (2)) and (ii) Brazier (M_{Bz} – k_{Bz}) moments – M_{Bz} is given by (Brazier 1927)

$$M_{Bz}=\frac{2\sqrt{2}}{9}\frac{E\pi rt^2}{\sqrt{1-v^2}} \tag{6}$$

and k_{Bz} is obtained by solving the equation $M_{Bz}=\sigma_{cr}\,I/a$, setting $k=k_{Bz}$, which leads to

$$k_{Bz}=\frac{16\sqrt{2}\beta_2\sin\left(\frac{2\pi}{n}\right)\sqrt{1-v^2}}{\pi n\left(2+\cos\left(\frac{2\pi}{n}\right)\right)} \tag{7}$$

with the RCPS moment of inertia I and apothem a[7], given, respectively, by

$$I=\frac{r^2tbn}{6}\left(2+\cos\left(\frac{2\pi}{n}\right)\right) \tag{8}$$

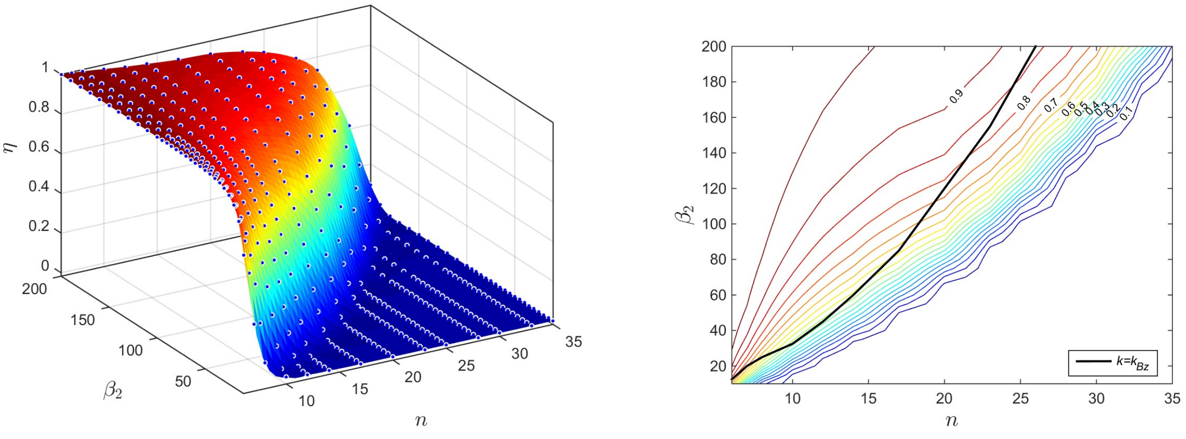

(a) (b)

Figure 2: Variation of η with n and β_2: (a) 3D and (b) 2D (η-isocurves) representations.

---

[7] Distance between the RCPS centre and any of its sides.

$$a = r\cos\left(\frac{\pi}{n}\right) \tag{9}$$

The thick black curve in Fig. 2(b) corresponds to $k=k_{Bz}$ and will be discussed in Section 3.3.

2.2 Beam geometry selection

A detailed analysis of the post-buckling behavior of beams with different geometries is carried out in Section 3 – the beams buckle in local, distortional or mixed local-distortional modes. The beam geometry selection is discussed next and the chosen geometries are provided in Table 1 (n,r,b,t,L values), together with the associated β_2, η, critical buckling stress (σ_{cr}) and critical mode half-wave number (n_{cr}) values. For the beams buckling in pure local modes (η close to 1.0), analyzed in Section 3.1, the cross-sections selected correspond to (i) n=6 with β_2=100 (η=0.996) and (ii) n=8 with β_2=50 (η=0.875) – in each case, two lengths are considered to assess the influence of the beam length (beams 1 to 4 in Table 1). As for the beam geometries chosen to assess the pure distortional post-buckling behavior, in Section 3.2, they have η values close to 0.0 and correspond to (i) n=14 with β_2=20 (η=0.00), (ii) n=20 with β_2=20 (η=0.00) and (iii) n=30 with β_2=20 (η=0.00) – two lengths are considered for n=14 and n=20, but only one for n=30 (beams 9, 10, 14, 15, 16 in Table 1). Lastly, two beam geometry sets were chosen to study, in Section 3.3, the local-distortional interactive post-buckling behavior: (i) n=10 with β_2=20 (η=0.143), 35 (η=0.515), 50 (η=0.717), 65 (η=0.820), and (ii) n=14 with β_2=40 (η=0.154), 60 (η=0.532), 100 (η=0.825) – a single length is considered in all cases (beams 5-8 and 11-13 in Table 1). Although the beams exhibiting n=10 with β_2=65 and n=14 with β_2=100 buckle in almost "pure local modes" (η close to 1.0), their structural response is included in Section 3.3 to assess, as thoroughly as possible, all beam post-buckling behaviors.

Table 1: Selected RCPS beam geometries (n, r, b, t, L) and η, β_2, critical stress σ_{cr}) and critical half-wave number (n_{cr}) values.

Beam	n	r (mm)	b (mm)	t (mm)	β_2	η	L (mm)	σ_{cr} ($kNcm$)	n_{cr}
1	6	100	100.0	1.00	100	0.996	500.0	95.75	6
2	6	100	100.0	1.00	100	0.996	1500.0	96.21	17
3	8	125	95.7	2.50	50	0.875	700.0	15.61	8
4	8	125	95.7	2.50	50	0.875	187.5	15.66	22
5	10	100	61.8	5.00	20	0.143	700.0	258.94	12
6	10	100	61.8	2.86	35	0.515	700.0	52.75	12
7	10	100	61.8	2.00	50	0.717	700.0	18.42	12
8	10	100	61.8	1.54	65	0.820	700.0	8.44	12
9	14	100	44.5	5.00	20	0.004	300.0	325.13	7
10	14	100	44.5	5.00	20	0.004	600.0	322.90	14
11	14	100	44.5	2.50	40	0.154	600.0	62.05	14
12	14	100	44.5	1.67	60	0.532	600.0	19.36	14
13	14	100	44.5	1.00	100	0.825	600.0	4.27	14
14	20	100	31.3	5.00	20	0.000	200.0	331.62	5
15	20	100	31.3	5.00	20	0.000	1000.0	331.05	24
16	30	125	26.1	6.25	20	0.000	1250.0	430.02	24

2.3 GBT-assessment of selected beams

The GBT-based characterization of the bucking (bifurcation) behavior of most selected RCPS beams is addressed next. Recall that all the beams considered in this work are simply supported (end cross-sections locally/globally pinned and free to warp), unrestrained along the longitudinal direction[8] and subjected to

---

[8] No ring stiffeners inhibiting/restraining ovalization and cross-section distortion are considered here – nevertheless, it should be noted that they constitute an excellent option in practical applications.

uniform bending causing uniform compression at the top horizontal wall. GBT linear stability analyses have been amply discussed and employed in the past – detailed descriptions of the procedures involved in determining the deformation modes (*cross-section analysis*) and solving the system of differential adjacent equilibriums equations (*member buckling analysis*) can be found in the literature (*e.g.*, Gonçalves *et al*. 2014 and Bebiano *et al*. 2015). For illustrative purposes, Figs. 3(a)-(b) and 4(a)-(b) show the GBT deformation modes of (i) n=8 RCPS (beams 3, 4 in Table 1) and (ii) n=20 RCPS (beams 14, 15 in Table 1), employing the cross-section discretizations[9] also depicted at the top left-hand sides of those figures. These discretizations lead to (i) 24 (4 global, 5 distortional and 15 local) or 26 (4 global, 17 distortional and 5 local) conventional modes – modes **1-24** (Fig. 3(a)) or modes **1-26** (Fig. 4(a)), (ii) 22 (7 global and 18 local) or 24 (19 global and 5 local) shear modes – modes **25-46** (Fig. 3(b)) or modes **27-50** (Fig. 4(b)), (iii) 23 (1 global isotropic, 5 global deviatoric, 2 distortional and 15 local) or 25 (1 global isotropic, 17 global deviatoric, 2 distortional and 5 local) linear transverse extension modes – modes

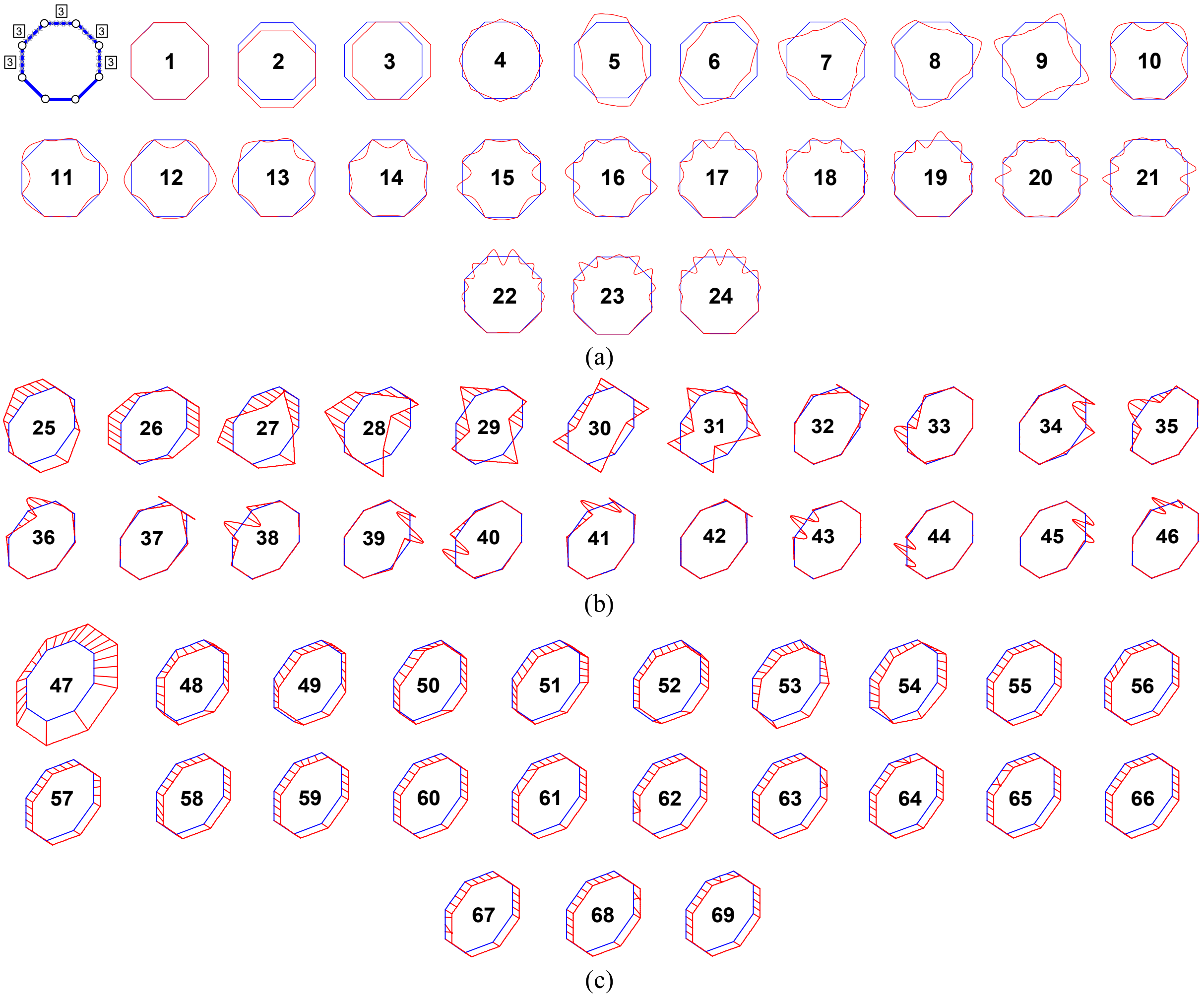

Figure 3: (a) GBT discretisation and conventional deformation modes, (b) shear mode warping displacement profiles and (c) linear transverse extension deformation modes of the RCPS with n=8, r=125mm and t=2.5mm.

---

[9] The cross-section discretizations employed correspond to those needed to obtain accurate GBT-based geometrically non-linear results, which will be discussed in the next sections – in the context of GBT buckling (linear stability) analysis, less refined cross-section discretizations may suffice to obtain similarly accurate results. Note that the discretiztion is only refined in the cross-section compressed half, thus making it possible to capture the relevant non-linear effects without increasing unnecessarily the computational effort.

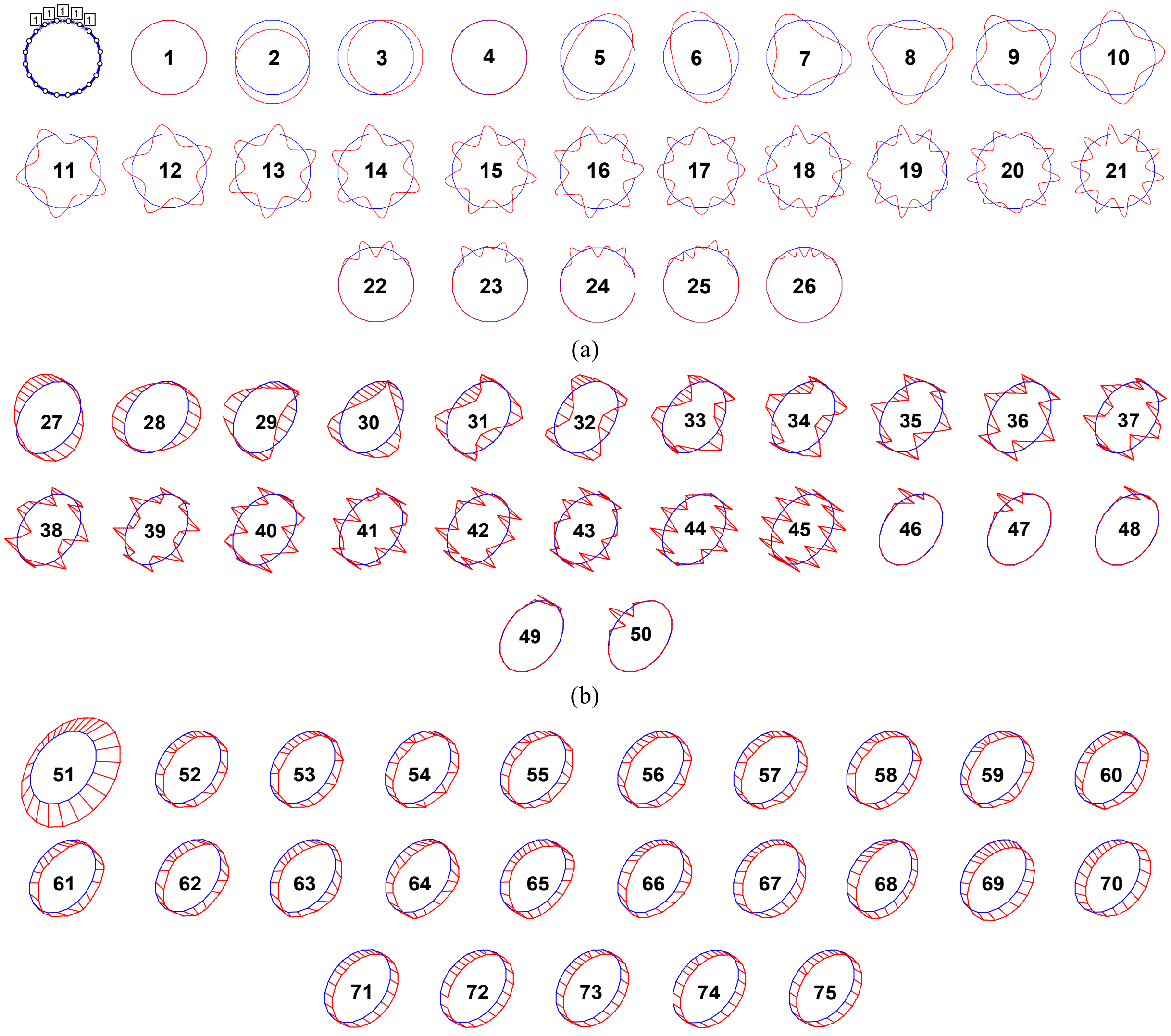

(a) (b) (c)

Figure 4: (a) GBT discretization and conventional deformation modes, (b) shear mode warping displacement profiles and (c) linear transverse extension deformation modes of the RCPS with *n*=20, *r*=100mm and *t*=5.0mm.

47-69 (Fig. 3(c)) or modes **51-75** (Fig. 4(c)), and (iv) 23 or 25 quadratic transverse extension modes (not shown in this work).

Figs. 5(a_1)-(a_9) display the critical[10] buckling mode shapes of most of the beams characterized in Table 1, which will be used as initial geometrical imperfections in the geometrically non-linear analyses with imperfections (GNIA) addressed in subsequent sections – the critical stress values (σ_{cr}) have already been given in Table 1. On the other hand, Figs. 5(b_1)-(b_9) show the associated GBT modal amplitude functions (conventional and transverse extension modes) or its derivatives (shear modes), *i.e.*, the contributions of each GBT deformation mode to the beam buckling mode (x is the longitudinal coordinate – $0 \leq x \leq L$). Naturally, due to the lack of rotational symmetry of the cross-section deformation, RCPS beams involve a much higher number of modes than their column counterparts (*e.g.*, Martins *et al.* 2019a,b). Nonetheless,

---

[10] The sole exception concerns beam 10 (*n*=14, *L*=600mm), for which the first non-critical buckling modes and associated modal amplitude function is also shown in Figs. 5(a_7)+(b_7) (see discussion in Section 3.2).

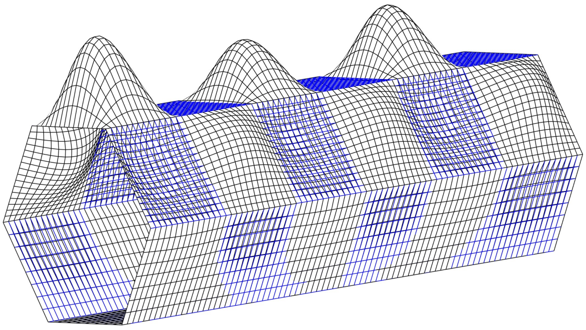

(a$_1$)

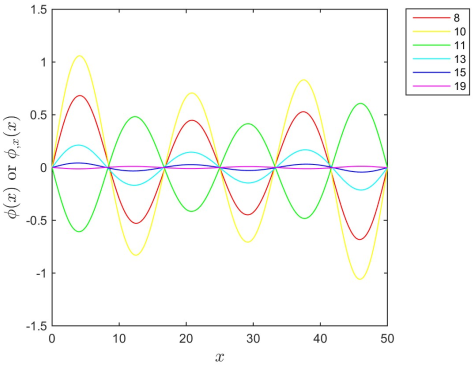

(b$_1$)

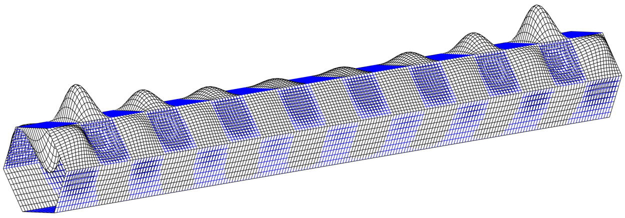

(a$_2$)

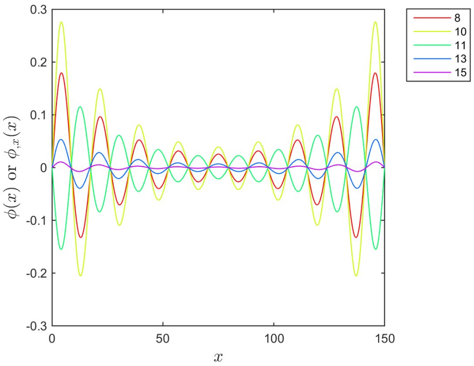

(b$_2$)

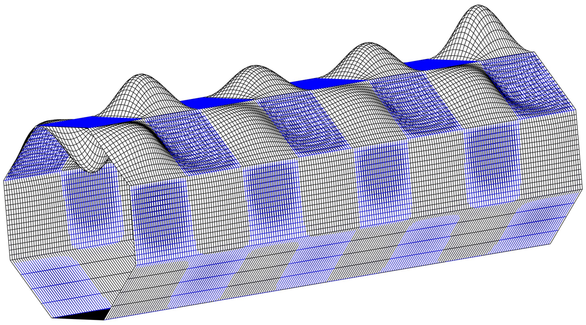

(a$_3$)

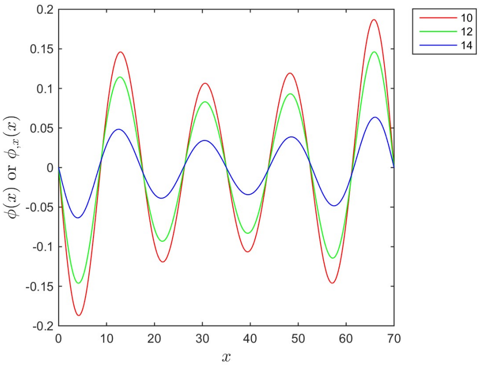

(b$_3$)

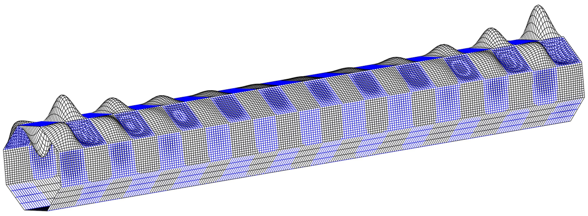

(a$_4$)

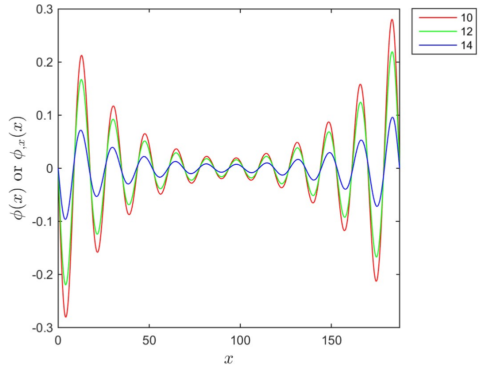

(b$_4$)

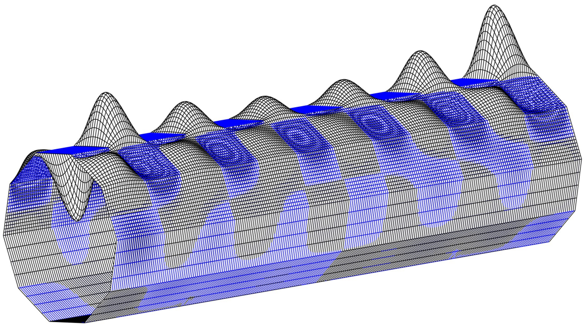

(a$_5$)

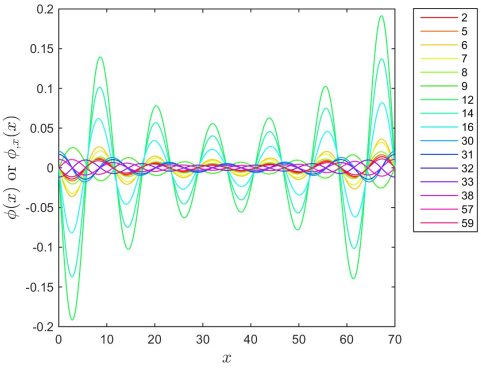

(b$_5$)

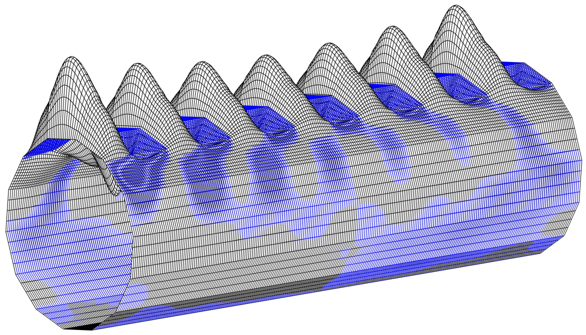

(a$_6$)

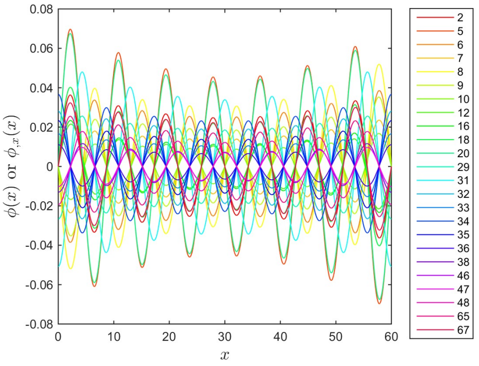

(b$_6$)

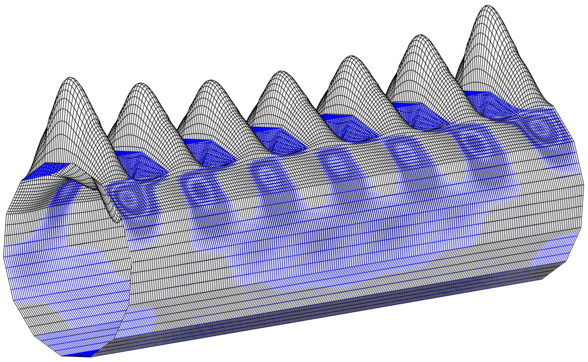

(a$_7$)

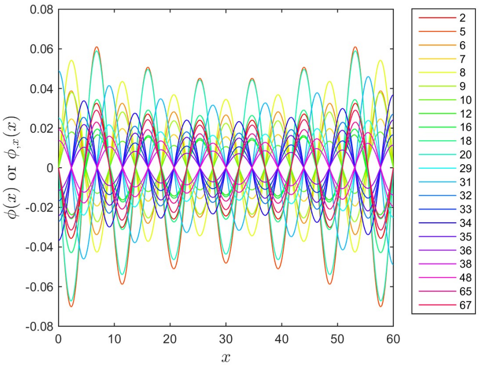

(b$_7$)

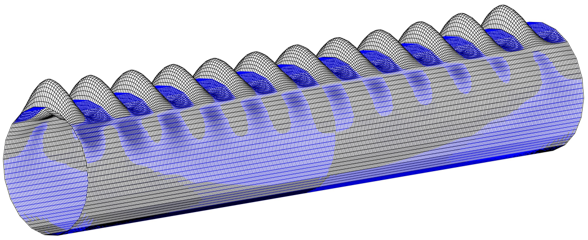

(a$_8$)

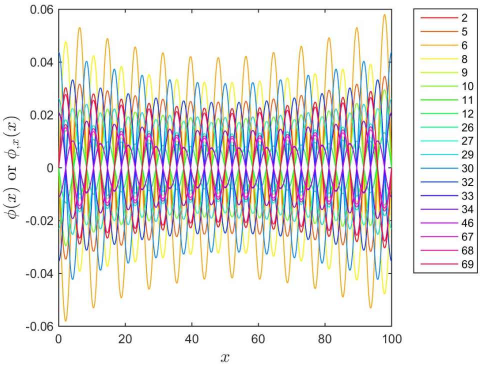

(b$_8$)

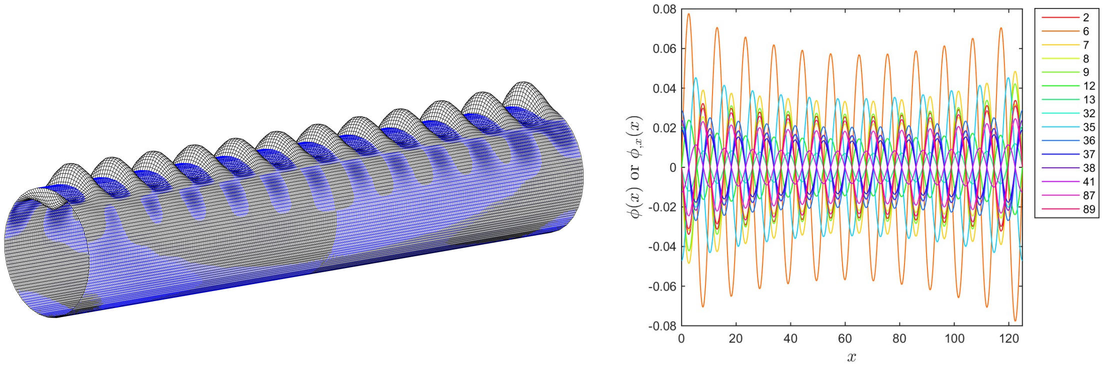

(a_9) (b_9)

Figure 5: GBT (a) buckling mode shapes and (b) associated modal amplitude functions of RCPS beams with ($_1$) n=6+L=50cm, ($_2$) n=6+L=150cm, ($_3$) n=8+L=70cm, ($_4$) n=8+L=187.5cm, ($_5$) n=10+L=70cm, ($_6$) n=14+L=60cm, ($_7$), n=14+L=60cm (first non-critical buckling mode), ($_8$) n=20+L=100cm, and ($_9$) n=30+L=125cm.

the number of deformation modes is much lower in the n=6 and n=8 beams (buckling in local modes), since only a few local deformation modes are required – *e.g.*, see Figs. 5(b_1)-(b_4). The remaining beams require also the consideration of shear and transverse extension deformation modes, with relevant participations in the beam buckling modes (*e.g.*, Figs. 5(b_5)-(b_9)). It is still worth mentioning that (i) due to end effects caused by the applied moment localization and Poisson's effect restraint, the half-wave amplitude is significantly higher at these regions, especially in beams buckling local modes, (ii) all beams have their first two bifurcation moments very close (they are associated with consecutive longitudinal half-wave numbers), and (iii) the distortional longitudinal half-wavelengths are much lower than their local counterparts (unlike in open-section beams).

3. Post-Buckling Behavior

This section presents and discusses the post-bucking behavior of all the selected RCPS beams, using a geometrically non-linear GBT finite element formulation extensively employed to acquire in-depth knowledge about the mechanics underlying several thin-walled member geometrically non-linear behaviors – *e.g.*, local, distortional, global or coupled ones (*e.g.*, Martins *et al.* 2018c, 2019a,b, Gonçalves & Camotim 2011, 2012). The presentation of the results begins with RCPS beams buckling in local modes (n=6+β_2=100 and n=8+β_2=50 – Section 3.1), followed by RCPS beams buckling in distortional modes (n=14+β_2=20, n=20+β_2=20 and n=30+β_2=20 – Section 3.2) and ends in Section 3.3 with the results of beams undergoing local-distortional interaction (n=10+β_2={20,35,50,65} and n=14+β_2={40,60,100}). All GBT results are (i) obtained with n_e equal-length finite elements, the cross-section discretizations shown in Fig. 6 and using an arc-length control strategy with small arc-length values (a critical issue, as

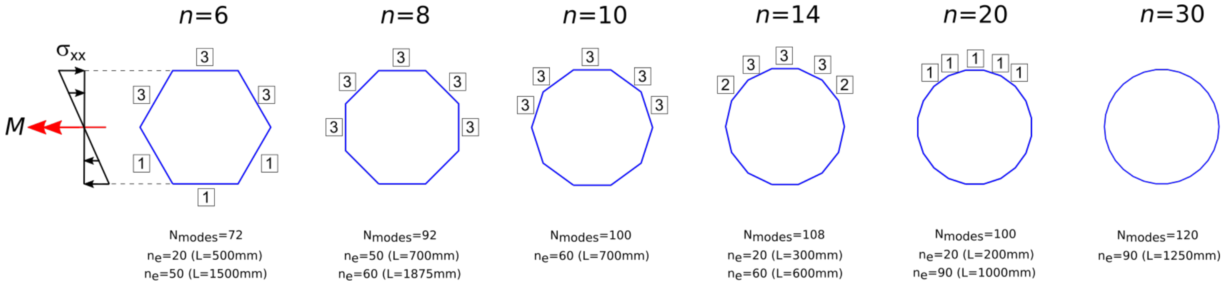

Figure 6: GBT cross-section and longitudinal discretizations adopted in all the RCPS beams investigated in this work.

discussed ahead), and (ii) validated through the comparison with values yielded by ABAQUS (Simulia Inc 2009) SFEA involving very refined S8R5 element meshes. Each beam geometry is analyzed with several initial geometrical imperfection amplitudes (to assess the imperfection sensitivity), namely (i) 0.01, 0.1, 0.2 and 0.5mm (beams buckling in local modes), and (ii) 0.1, 0.2 and 0.5mm (remaining beams). Finally, it is still worth noting that the results obtained are also compared with the corresponding Brazier moments.

3.1 Local post-buckling behavior

Figs. 7(a)-(b) show GBT and ABAQUS SFEA equilibrium paths M/M_{cr} vs. $(w+w_0)/t$, where w is the mid-span flexural displacement at the top wall mid-point caused by the applied moment M, of n=6+β_2=100 RCPS beams with 0.01, 0.1, 0.2 and 0.5mm critical-mode initial geometrical imperfection amplitudes, and lengths L=5r (beam 1 in Table 1) and L=15r (beam 2 in Table 1) – in the latter case, because the critical buckling mode shape has an odd half-wave number, initial geometrical imperfections with positive and negative amplitudes (of identical magnitude) were considered. Figs. 8(a)-(b) include a similar set of results for the n=8+β_2=50 RCPS beams (beams 3, 4 in Table 1). Note that (i) the bottom right-hand side of each graph shows the adopted initial geometrical imperfection 2D shape and the longitudinal location of its maximum amplitude[11], (ii) Fig. 8(a) shows only SFE results for the beams with 0.01 and 0.5mm initial imperfections (to improve readability) and (iii) Fig. 8(b) plots only SFE results of the beam 4 with the 0.5mm initial imperfection (the equilibrium paths of beam 4 virtually coincide for the 4 amplitudes considered – see the discussion below). As for Figs. 9(a)-(b), they show the GBT modal amplitude diagrams (p_j vs. M/M_{cr}), quantifying the relative importance of each deformation mode (or mode set) along the equilibrium paths of (i) beam 2 (n=6, β_2=100, t=1.0mm and L=15r) with the −0.2mm initial imperfection, and (ii) beam 4 (n=8, β_2=50, t=2.5mm and L=15r) with the 0.5mm initial imperfection. Figs. 10(a)-(e) and 11(a)-(e) provide the evolution, along the two beam equilibrium paths displayed in Figs. 9(a)-(b), of the modal contributions to the longitudinal profile of the top wall mid-point transverse displacement ($w(x)$), namely contributions from the (i) major-axis flexural mode **2** ($w_2(x)$ – Figs. 10(a) and 11(a)), (ii) distortional modes **5-7** ($w_{5\text{-}7}(x)$ – Fig. 10(b)) or **5-9** ($w_{5\text{-}9}(x)$ – Fig. 11(b)), (iii) local modes **8-19** ($w_{8\text{-}19}(x)$ – Fig. 10(c)) or **10-24** ($w_{10\text{-}24}(x)$ – Fig. 11(c)), (iv) transverse extension modes **37-54** ($w_{37\text{-}54}(x)$

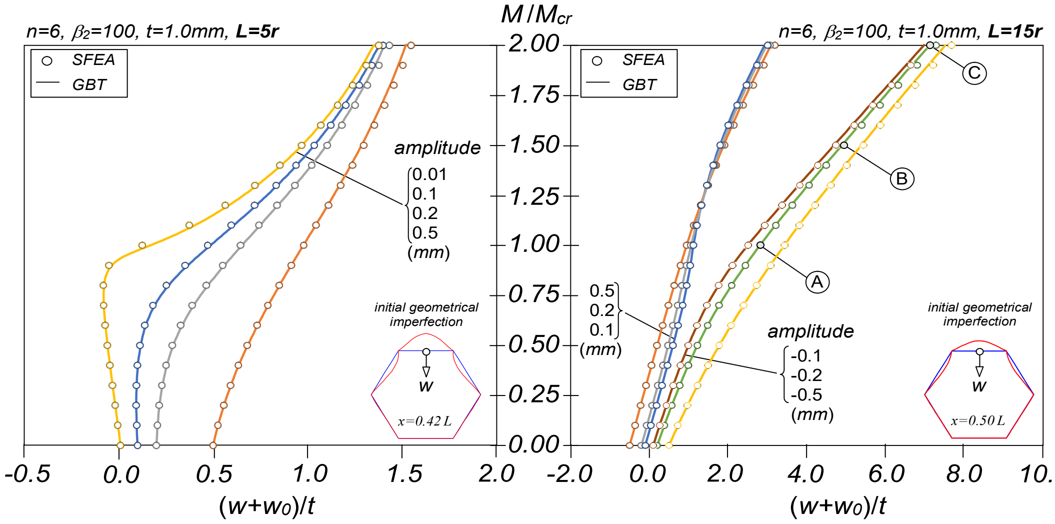

(a) (b)

Figure 7: Post-buckling equilibrium paths M/M_{cr} vs. $(w+w_0)/t$ of RCPS (n=6, β_2=100, t=1.0mm) beams containing critical-mode initial geometrical imperfections having several amplitudes and with two lengths: (a) L=5r and (b) L=15r.

---

[11] This information is included in all figures containing beam equilibrium paths.

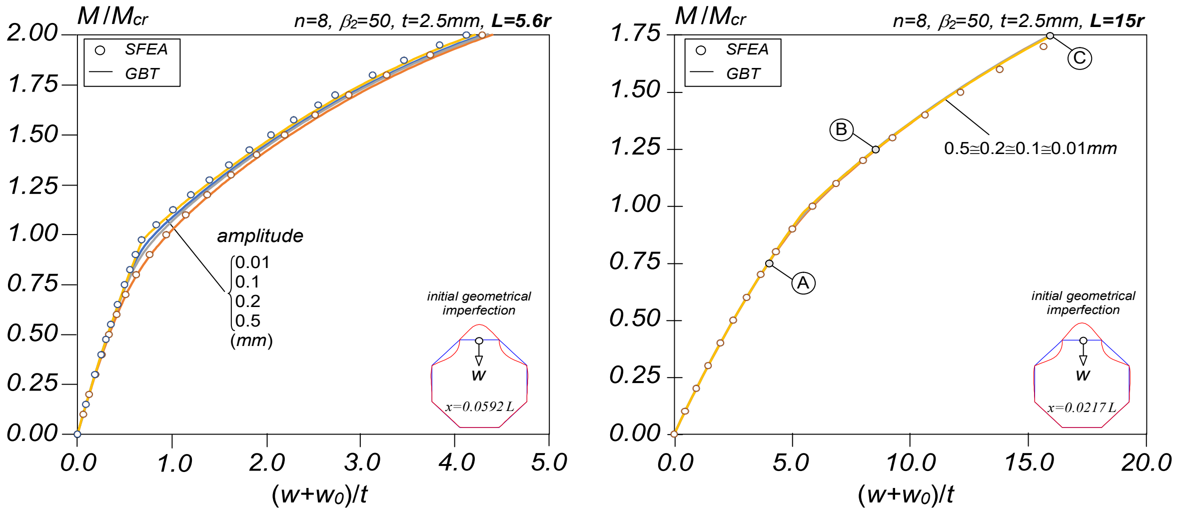

(a) (b)

Figure 8: Post-buckling equilibrium paths M/M_{cr} vs. $(w+w_0)/t$ of RCPS (n=8, β_2=50, t=2.5mm) beams containing critical-mode initial geometrical imperfections having several amplitudes and with two lengths: (a) L=5.6r and (b) L=15r.

– Fig. 10(d)) or **47-69** ($w_{47\text{-}69}(x)$ – Fig. 11(d)) and (v) all modes **1-72** ($w_{1\text{-}72}(x)$ – Fig. 10(e)) or **1-92** ($w_{1\text{-}92}(x)$ – Fig. 11(e)). Lastly, Figs. 12(a)+(b) show GBT-based deformed configurations of the two above beams at equilibrium states located on their equilibrium paths plotted in Figs. 7(b) and 8(b), identified by "A", "B" and "C". The observation of all these local post-buckling results leads to the following comments:

(i) Despite the disparity between the DOF numbers involved, there is an excellent agreement between the GBT and ABAQUS SFE results for all the beam equilibrium paths plotted in Figs. 7(a)-(b) and 8(a)-(b), up to either M/M_{cr}=2.00 (Figs. 7(a)-(b) and Fig. 8(a)) or M/M_{cr}=1.75 (Fig. 8(b)).

(ii) As expected, Figs. 7(a)-(b) and 8(a)-(b) show that, regardless of the initial geometrical imperfection amplitude, the beams exhibit stable equilibrium paths with very pronounced post-critical strengths[12], a feature invariably associated with local post-buckling. Fig. 12 provides visual confirmation of the locally buckled beam deformed configurations.

(iii) The comparison between the modal participation diagrams displayed in Figs. 9(a)-(b) shows a few similarities, namely a dominant contribution from the flexural mode **2**[13] and relevant participations of some local and distortional modes along both equilibrium paths. Indeed, p_2 decreases from 74.3% to 51.5% (Fig. 9(a)) or from 95.9% to 54.3% (Fig. 9(b)) while, conversely, the remaining modal contributions increase. The distortional mode contribution consists mostly of mode **5** (beam 2) or modes **5**+**6** (beam 4), with a tiny contribution from mode **6** (beam 2) or modes **7**+**8** (beam 4), while modes **7** or **9** do not contribute – p_5 and p_6 reach maximum values of 14.0% and 2.8% (Fig. 9(a) at M/M_{cr}=2.00) or 18.0% and 7.6% (Fig. 9(b) at M/M_{cr}=1.75), respectively. Concerning the local deformation modes, a significant number have very small participations. Indeed, modes **8**+**10**+**11** are the most relevant in beam 2 (particularly the first two), while in beam 4 this role is played by

---

[12] Note that Fig. 7(b) shows a pronounced difference between the equilibrium paths concerning positive and negative initial imperfection amplitudes. However, the post-buckling behaviors of the two beams are very similar. This is not perceptible in Fig. 7(b) because the two equilibrium paths plot the maximum mid-span (x/L=0.5) displacement, whereas the absolute maximum displacement occurs (i) at x/L=0.44 and x/L=0.56 (half-waves adjacent to the mid-span one), for the beams with positive initial imperfection amplitudes, and (ii) at mid-span, for the beams with negative initial imperfection amplitudes.

[13] Note that the applied bending moment compresses uniformly the top wall. Any other moment orientation would lead to a linear combination between the flexural modes **2** and **3**.

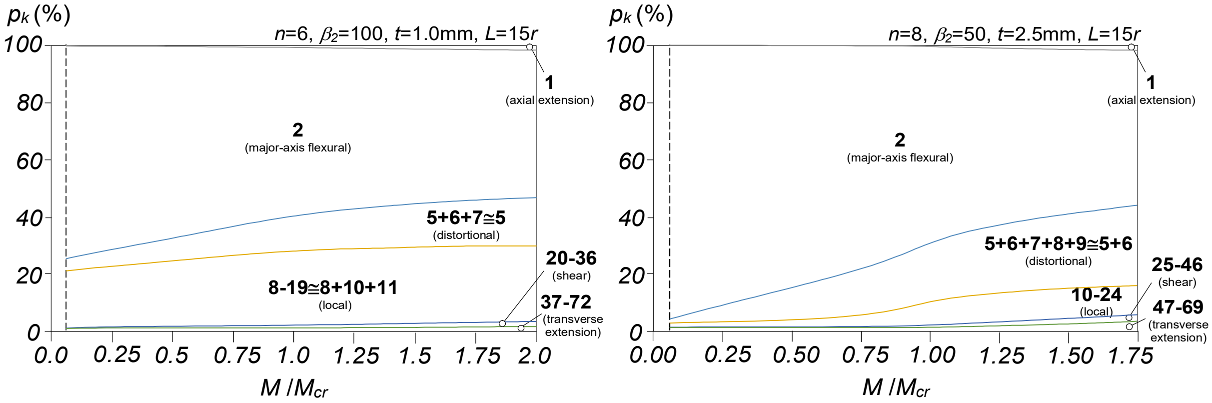

(a) (b)

Figure 9: Modal participation diagrams p_k vs. M/M_{cr} of (a) beam 2 (n=6, β_2=100, t=1.0mm and L=15r) with the –0.2mm initial imperfection and (b) beam 4 (n=8, β_2=50, t=2.5mm and L=15r) with the 0.5mm initial imperfection.

modes **10**+**12** (naturally, this same feature is also observed in the beam buckling modes – see Figs. 5(b_2)+(b_4)) – the other local modes have participations not exceeding 1%. The joint contribution from the shear and transverse extension modes never exceeds 3.5% (beam 2) or 6.0% (beam 4) but involves several modes. For instance, in beam 4 the most relevant shear and transverse extension modes (see Fig. 3(b)-(c)) are **25**+**27**+**36**+**28**+**29**+**32**+**35** and **55**+**56**+**47**+**64**+**53**+**51**+**57**+**58**+**60-63**, respectively – in both cases, these modes are ordered by descending modal contribution.

(iv) The analysis of the longitudinal profiles displayed in Figs. 10(a)-(e) and 11(a)-(e) shows that all modal contributions retain more or less their configurations along the equilibrium paths. Indeed, $w_2(x)$ retains a single half-wave sinusoidal shape, due the simply supported boundary conditions, and only becomes very slightly "wavy" at advanced post-buckling stages – *e.g.*, see the displacement profiles at M/M_{cr}=2.007 (Fig. 10(a)) or M/M_{cr}=1.747 (Fig. 11(a)). The $w_{5\text{-}7}(x)$ or $w_{5\text{-}9}(x)$, providing the distortional contribution to $w(x)$ and practically absent from the critical local buckling mode (see Figs. 5(b_1)+(b_4)), also retain their configurations, but become much more "wavy" for M/M_{cr}>1.0. At this stage, it is worth noting that the distortional mode contribution is significantly higher in beam 4 (n=8+β_2=50) than in beam 2 (n=6+β_2=100) (see Figs. 9(a)-(b)), which indicates that the Brazier effect (ovalization) becomes more relevant as n increases – this issue will be amply discussed in the next sections. While it is fair to say that ovalization does not play a relevant role in the n=6 beams, the amount of ovalization occurring in the n=8 beams (see the 2D mid-span configuration in Fig. 12(b_3)) is responsible for the less stable equilibrium paths exhibited by these beams – compare the post-critical strengths of the n=6 and n=8 beams in Figs. 7(a)-(b) and 8(a)-(b). The $w_{8\text{-}19}(x)$ or $w_{10\text{-}24}(x)$ profiles, showing the local mode contributions to $w(x)$, retain their shapes, akin to the initial geometrical imperfections, while the amplitudes grow as the applied moment increases. Lastly, the $w(x)$ curves (Figs. 10(e) and 11(e)), which combine relevant contributions from $w_2(x)$+$w_{8\text{-}19}(x)$ or $w_2(x)$+$w_{5\text{-}9}(x)$+$w_{10\text{-}24}(x)$, characterize the local post-buckling behavior of the two beams, which is also clearly illustrated by the 3D and 2D configurations shown in Figs. 12(a_1)-(b_3).

(v) The comparison between the equilibrium paths displayed in Figs. 7(a)-(b) and 8(a)-(b) that concern beams differing only in the length unveils significant stiffness erosion as the length increases, which is due to the Brazier effect. Nonetheless, all the beams exhibit, to a larger or smaller extent, very high post-critical strengths (note that M_{Bz}/M_{cr} is well above 2.0, which means that the Brazier effect is only relevant for applied moments much higher than the critical bifurcation moment).

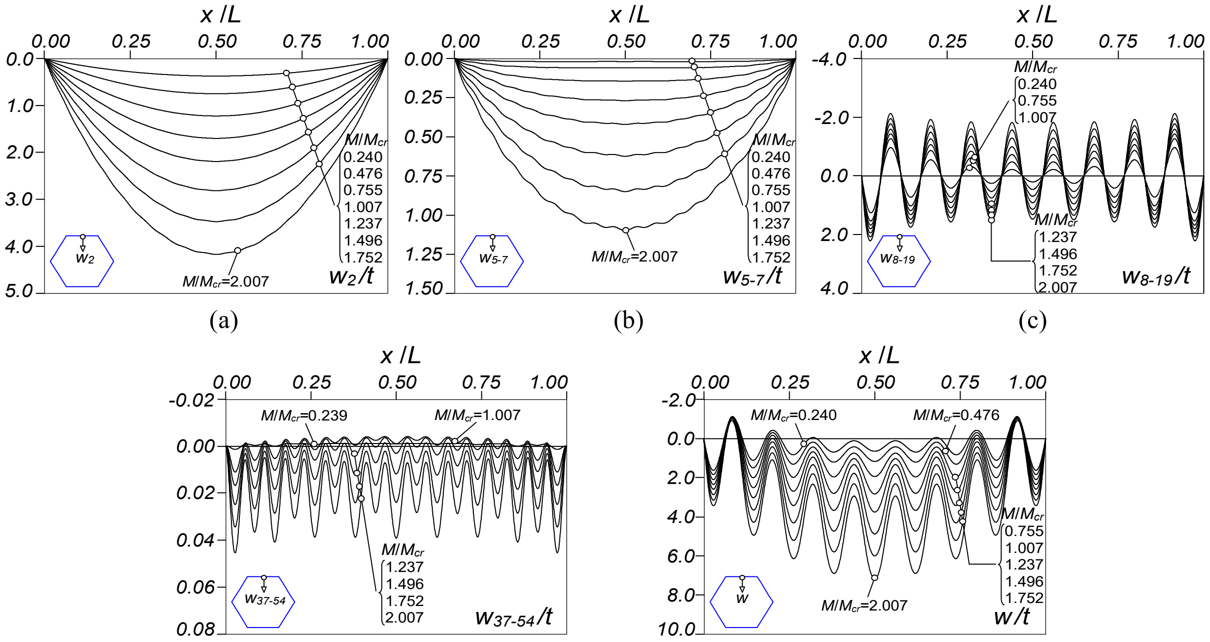

(a) (b) (c)

(d) (e)

Figure 10: Longitudinal displacement profiles of the RCPS (n=6, β_2=100, t=1.0mm and L=15r) beam with the –0.2mm initial imperfection: (a) $w_2(x)$, (b) $w_{5\text{-}7}(x)$, (c) $w_{8\text{-}19}(x)$, (d) $w_{37\text{-}54}(x)$, and (e) $w_{1\text{-}72}(x)\equiv w(x)$.

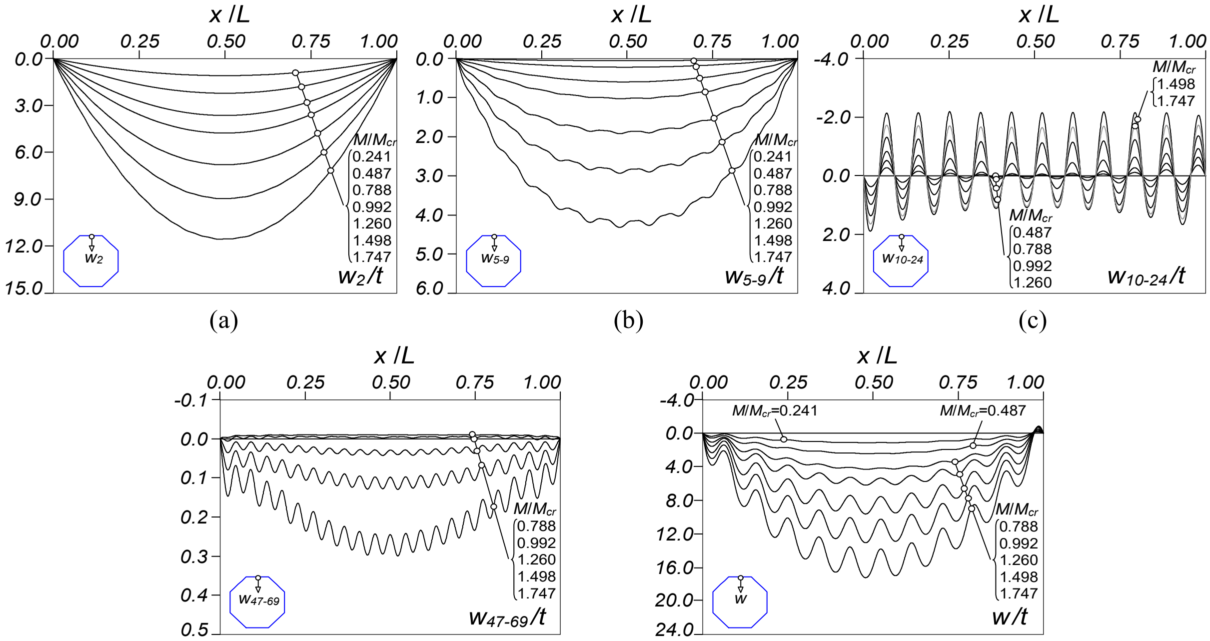

(a) (b) (c)

(d) (e)

Figure 11: Longitudinal displacement profiles of the RCPS (n=8, β_2=50, t=2.5mm and L=15r) beam with the 0.5mm initial imperfection: (a) $w_2(x)$, (b) $w_{5\text{-}9}(x)$, (c) $w_{10\text{-}24}(x)$, (d) $w_{47\text{-}69}(x)$, and (e) $w_{1\text{-}92}(x)\equiv w(x)$.

(vi) In the view of what was discussed, it is clear that the beams analyzed exhibit a *plate-like* behavior and, therefore, are able to sustain applied moments significantly above the critical buckling moment (assuming that the material behavior remains elastic, of course).

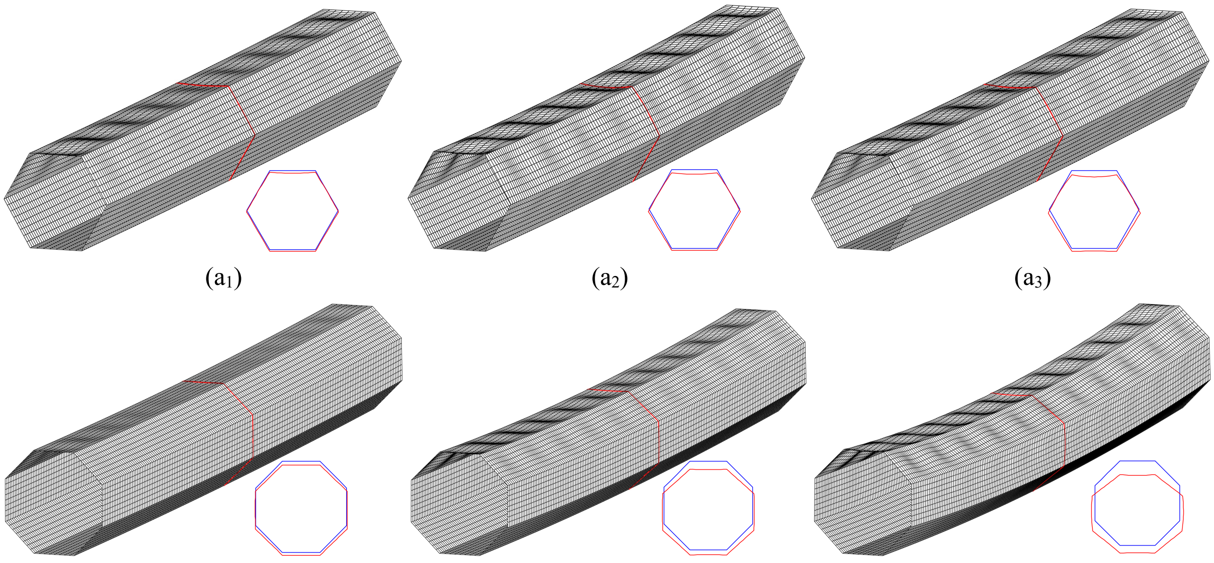

(a$_1$) (a$_2$) (a$_3$)

(b$_1$) (b$_2$) (b$_3$)

Figure 12: GBT-based deformed configurations of (a) beams 2 (n=6+β_2=100) and (b) beams 4 (n=8+β_2=50) at M/M_{cr} close to (a$_1$) 1.00, (a$_2$) 1.50 and (a$_3$) 2.00, and (b$_1$) 0.75, (b$_2$) 1.25 and (b$_3$) 1.75 (equilibrium states "A", "B" and "C" in Figs. 7(b) and 8(b)).

3.2 Distortional post-buckling behavior

Attention is now turned to RCPS beams with large wall numbers (n=14, n=20 and n=30, all with β_2=20). Unlike in the beams discussed in the previous section, buckling now involves non-null displacements of the wall ends/corners. Figs. 13(a$_1$)-(b$_2$) show GBT and ABAQUS SFEA M/M_{cr} vs. $(w+w_0)/t$ equilibrium paths (the latter for validation purposes only), where w is again the mid-span flexural displacement of the top wall mid-point, concerning two RCPS beam geometries, namely (i) n=14, β_2=20 and L=3r (beam 9 – Figs. 13(a$_1$)+(a$_2$)), and (ii) n=20, β_2=20 and L=2r (beam 14 – Figs. 13(b$_1$)+(b$_2$)), both containing critical-mode initial geometrical imperfections with six amplitudes w_0: +0.1, +0.2, +0.5mm (Figs. 13(a$_1$)+(b$_1$)) and –0.1, –0.2, –0.5mm (Figs. 13(a$_2$)+(b$_2$)) – note that the critical buckling mode exhibits an odd half-wave number in both beams. As for Figs. 14(a$_1$)-(b), they concern solely n=14+β_2=20 RCPS beams (same cross-section dimensions), but with twice the length considered before (*i.e.*, L=6r). In these beams, two initial geometrical imperfection shapes were considered, with identical amplitudes (0.1, 0.2, 0.5mm): imperfections akin to the (i) first bifurcation mode (odd half-wave number − positive and negative imperfection amplitudes considered – see Figs. 14(a$_1$)+(a$_2$)) and (ii) second bifurcation mode (even half-wave number – see Fig. 14(b)). Fig. 15(a$_1$)-(b) shows modal participation diagrams p_k vs. M/M_{cr} or p_k vs. $(w+w_0)/t$ concerning the beams with +0.50mm (Figs. 15(a$_1$)+(a$_2$)) and –0.50mm (Fig. 15(b)) initial geometrical imperfections. Moreover, Figs. 16(a)-(e), 17(a)-(e) and 18(a)-(e) provide the evolution of the modal contributions to the top wall mid-point transverse displacement $w(x)$, for n=14+β_2=20 RCPS beams with +0.50mm (Figs. 16(a)-(e), 17(a)-(e)) and –0.50mm (Fig. 18(a)-(e)) initial imperfections[14]. These figures show the contributions from the (i) major-axis flexural mode **2** ($w_2(x)$ – Figs. 16-18(a)), (ii) distortional modes **5-15** ($w_{5\text{-}15}(x)$ – Figs. 16-18(b)), (iii) local modes **16-28** ($w_{16\text{-}28}(x)$ – Figs. 16-18(c)), (iv) linear transverse extension modes **55-81** ($w_{55\text{-}81}(x)$ – Figs. 16-18(d)) and (v) all modes **1-108** ($w_{1\text{-}108}(x)$ – Figs. 16-18(e)). Note that the symbol (↓) appearing in these figures identifies an equilibrium point located on the descending branch, *i.e.*, beyond the limit point. Lastly, Figs. 19(a$_1$)-(c$_3$) show 3D and 2D mid-span deformed configurations of the above n=14+β_2=20 beams at equilibrium states located on their

---

[14] Two beams but three equilibrium paths (see the discussion further ahead).

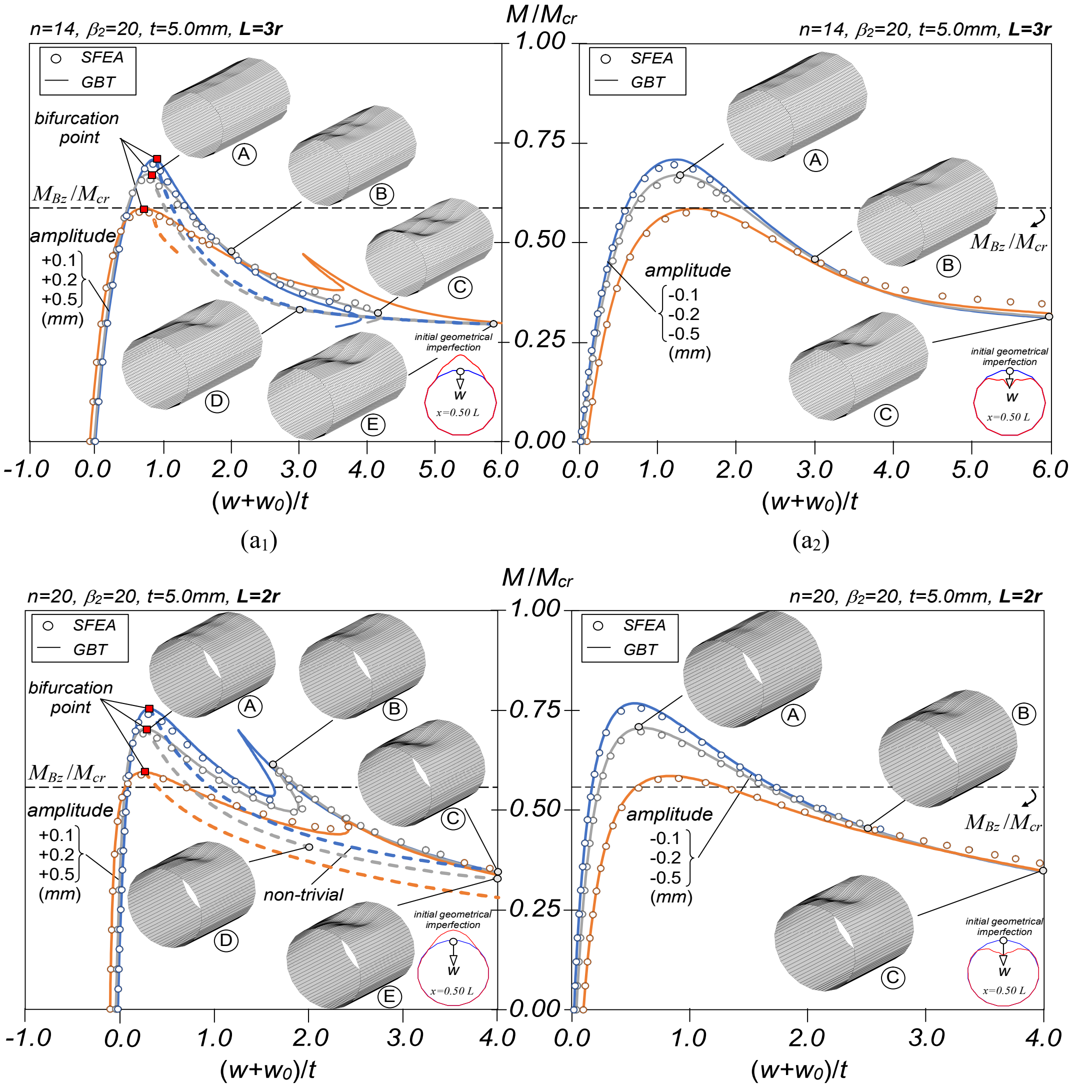

(a₁) (a₂)

(b₁) (b₂)

Figure 13: Post-buckling equilibrium paths M/M_{cr} vs. $(w+w_0)/t$ of beams with critical-mode initial geometrical imperfections having several ($_1$) positive or ($_2$) negative amplitudes: (a) n=14, β_2=20, t=5.0mm, L=3r, and (b) n=20, β_2=20, t=5.0mm, L=2r.

equilibrium paths plotted in Figs. 14(a$_1$)-(a$_2$), identified as points "A", "B", "C", "D", "E" and "F". The observation of all these distortional post-buckling results prompts the following remarks:

(i) All the equilibrium paths evidence that the distortional post-buckling behavior is remarkably distinct from its local counterpart, addressed in Section 3.1 – indeed, they are all unstable and imperfection sensitive. They all exhibit small initial linear regions, followed by significantly non-linear paths in which the stiffness is gradually eroded, due to the cross-section ovalization (reduces the moment of inertia), until an elastic limit point is invariably reached. Then, more or less smooth descending branches follow and, depending on the initial imperfection shape and/or the plotted displacement location, they may involve a clear snap-back. This post-buckling behavior is qualitatively similar to that exhibited by cylindrically tubes under bending (*e.g.*, Yadav & Gerasimidis 2019).

(ii) The beam equilibrium paths (post-buckling behaviors) plotted in (ii$_1$) Figs. 13(a$_1$) and 13(b$_1$) and (ii$_2$) Figs. 13(a$_2$) and 13(b$_2$) are remarkably similar. On the other hand, there are visible differences

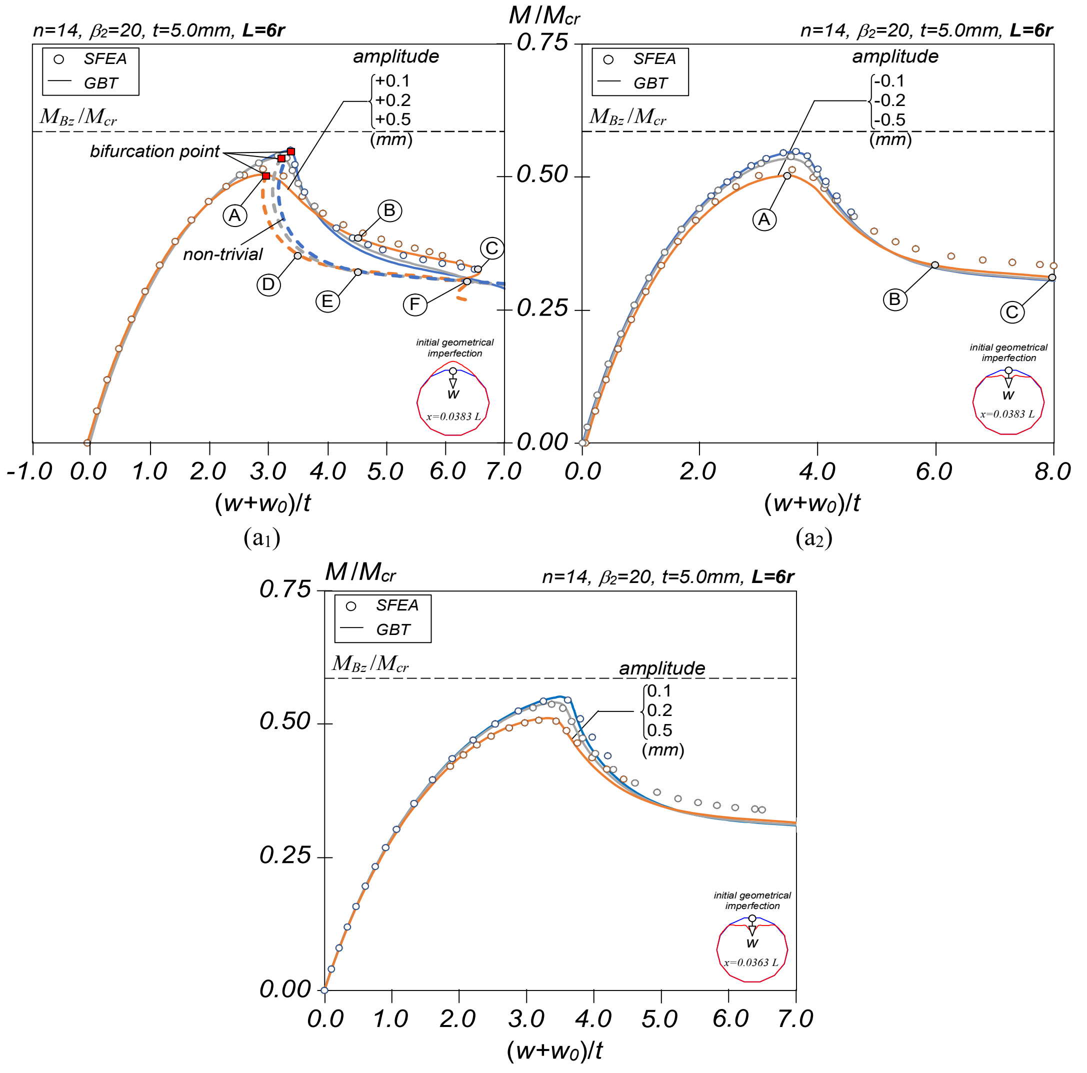

(a$_1$) (a$_2$)

(b)

Figure 14: Post-buckling equilibrium paths M/M_{cr} vs. $(w+w_0)/t$ of the RCPS beam (n=14, β_2=20, t=5.0mm and L=6r) with initial geometrical imperfections akin to the (a) first and (b) second bifurcation modes, and with (a$_1$) positive or (a$_2$) negative amplitudes.

between the equilibrium paths plotted in (ii$_1$) Figs. 13(a$_1$) and 13(a$_2$) and (ii$_2$) Figs. 13(b$_1$) and 13(b$_2$). This means that the initial imperfection "sign" influences the post-buckling behavior, even if no significant failure moment change is observed, which can be explained by the occurrence, for inward w_0, of coupling between the Brazier effect and the imperfection amplification – the equilibrium paths plotted in Figs. 13(a$_2$)+(b$_2$) exhibit larger displacements associated with the same applied moment.

(iii) As shown in Fig. 13(a$_1$) (and also in Fig. 13(b$_1$)) loss of uniqueness of the numerical solution occurs in the descending branch, immediately after the elastic limit point. Indeed, the performance of an eigenvalue analysis of the GBT tangent global stiffness matrix reveals two negative eigenvalues in that region, one corresponding to the limit point and the other to a bifurcation at a point located in the descending branch. Therefore, from the bifurcation points indicated in Figs. 13(a$_1$)+(b$_1$) emerge (iii$_1$) "trivial" or fundamental equilibrium paths (solid curves in Figs. 13(a$_1$)+(b$_1$)) and (iii$_2$) "non-trivial" or alternative equilibrium paths (dashed curves in Figs. 13(a$_1$)+(b$_1$)). The GBT "non-trivial" solutions were obtained by means of an *eigenvector injection* into the solution (*e.g.*, see Borst *et al.* 2012).

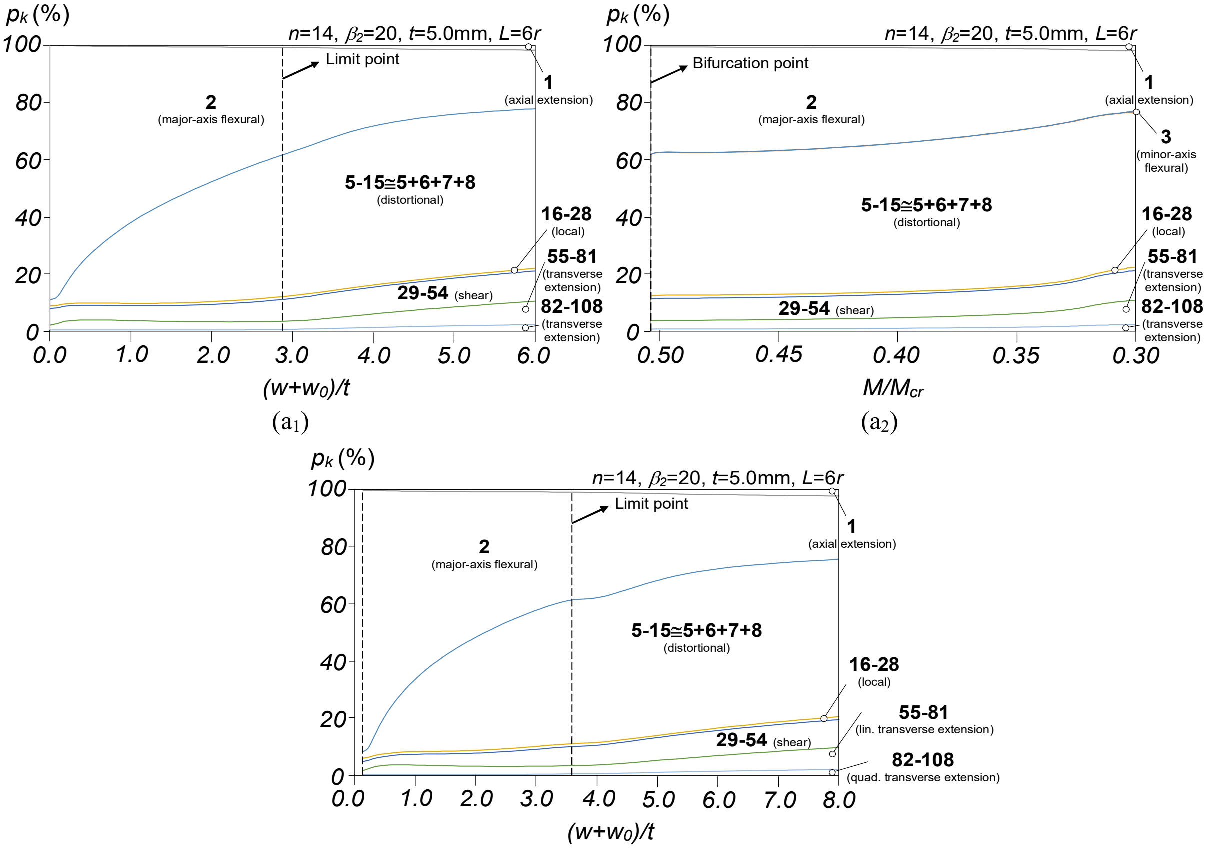

(a_1) (a_2)

(b)

Figure 15: Modal participation diagrams p_k vs. $(w+w_0)/t$ or p_k vs. M/M_{cr} of beam 10 (n=14, β_2=20 and L=6r) with critical-mode initial imperfections having amplitudes (a) +0.50mm ((a_1) trivial path or (a_2) non-trivial path) and (b) –0.50mm.

It is not possible to validate the "non-trivial" equilibrium paths obtained with GBT, since, to the authors' best knowledge, no branch switching techniques are implemented in ABAQUS. However, it was confirmed, through the *.msg* ABAQUS output file, that two negative eigenvalues exist near the bifurcation point detected by the GBT analysis. It is also worth noting that the computation of the non-trivial solutions requires the adoption of very small arc-length values in the vicinity of the limit point[15], in order to obtain the sequence of negative eigenvalue numbers: 0 (ascending branch), 1 (descending branch, immediately after the limit point and before the bifurcation point) and 2 (descending branch, after the bifurcation point), making the determination of the non-trivial paths straightforward – using larger arc-lengths entails a sequence 0-2 and "misses" the bifurcation point.

(iv) The post-buckling behaviors of the n=14+β_2=20 and n=20+β_2=20 beams with negative initial imperfections (Figs. 13(a_2)+(b_2)) are quite similar, as attested by comparing their equilibrium paths and deformed configurations (for w_0= –0.2mm) – this similarity does not exist for the (fundamental) equilibrium paths of the beams with positive initial imperfections (Figs. 13(a_1)+(b_1)). Indeed, regardless of the half-wave number (5 for L=2r or 7 for L=3r), the beam response gradually leads to the development of a localized "kink" at mid-span (symmetric deformation) combined with a clear reduction of the adjacent half-wave amplitudes. At fairly advanced post-buckling stages, the two

---

[15] The "in-house" GBT program is able to re-start/re-analyse the problem under scrutiny at any given equilibrium point, which is particularly useful in the situation described or, for instance, also when the solution of the quadratic arc-length equation does not provide a real solution.

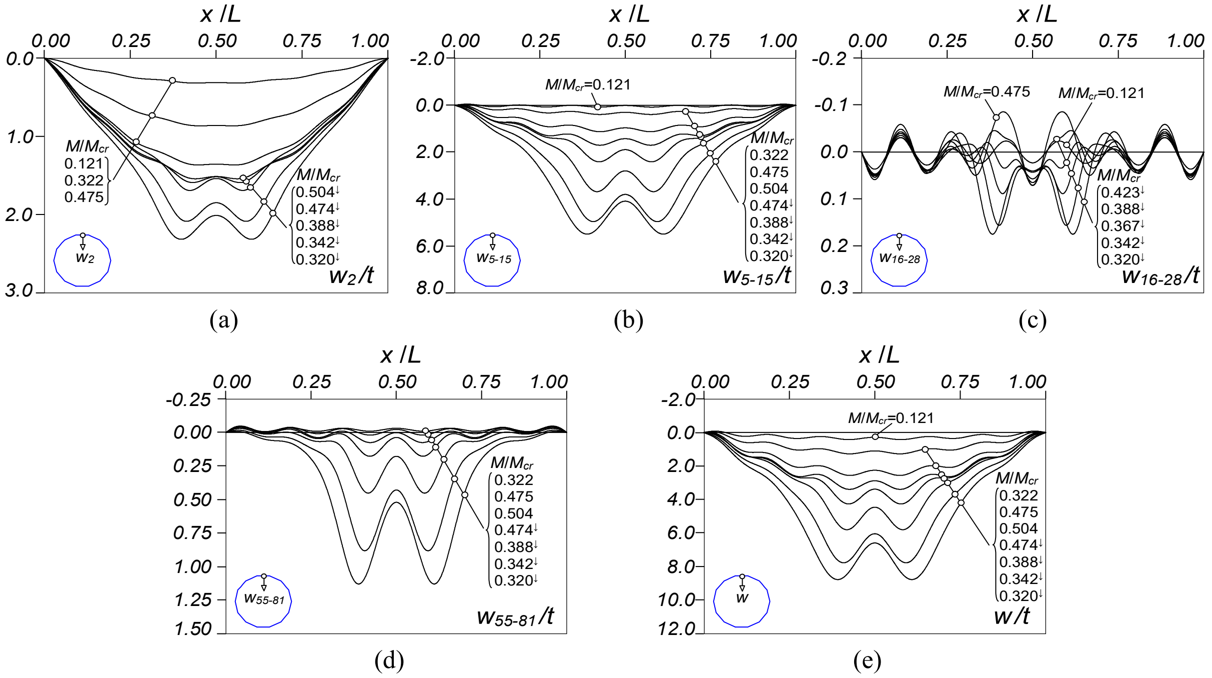

(a) (b) (c)

(d) (e)

Figure 16: Longitudinal displacement profiles of the RCPS (n=14, β_2=20, t=5.0mm, L=6r) beam with the +0.5mm initial imperfection (trivial path): (a) $w_2(x)$, (b) $w_{5\text{-}15}(x)$, (c) $w_{16\text{-}28}(x)$, (d) $w_{55\text{-}81}(x)$, and (e) $w_{1\text{-}108}(x)\equiv w(x)$.

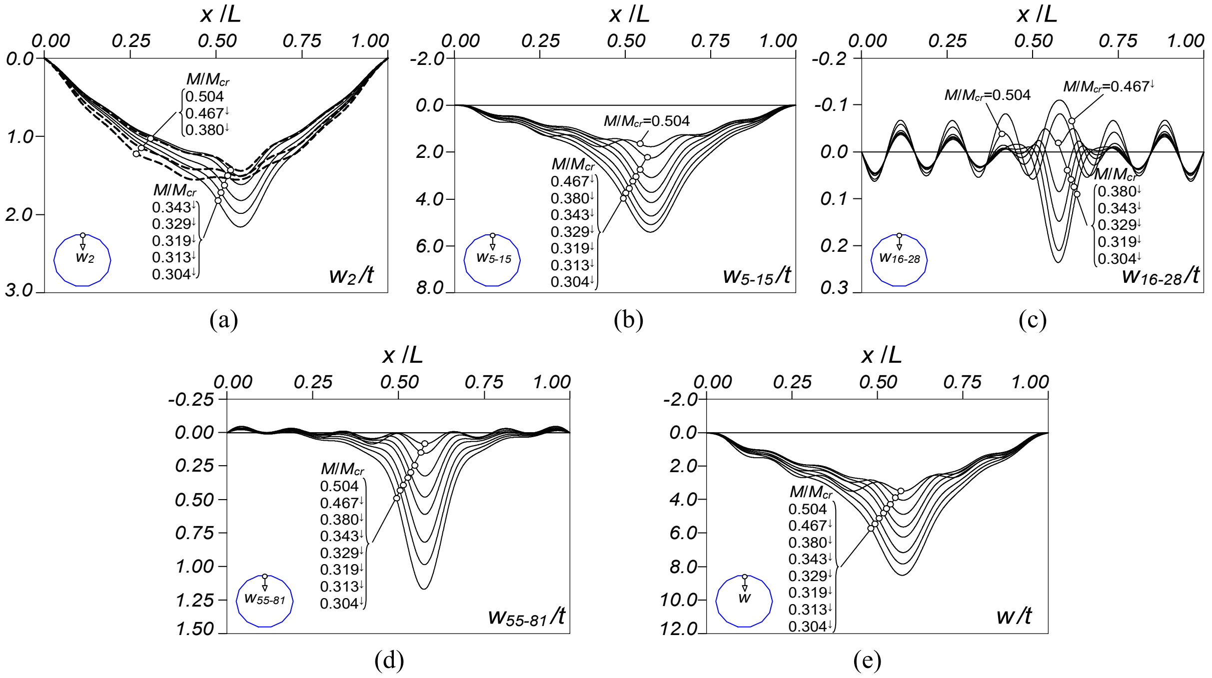

(a) (b) (c)

(d) (e)

Figure 17: Longitudinal displacement profiles of the RCPS (n=14, β_2=20, t=5.0mm, L=6r) beam with the +0.5mm initial imperfection (non-trivial path): (a) $w_2(x)$, (b) $w_{5\text{-}15}(x)$, (c) $w_{16\text{-}28}(x)$, (d) $w_{55\text{-}81}(x)$, and (e) $w_{1\text{-}108}(x)\equiv w(x)$.

equilibrium path trios practically merge into a common curve (see Figs. 13(a$_2$) and 13(b$_2$) for $(w+w_0)/t>3.0$ and 2.5, respectively), where no bifurcations were detected.

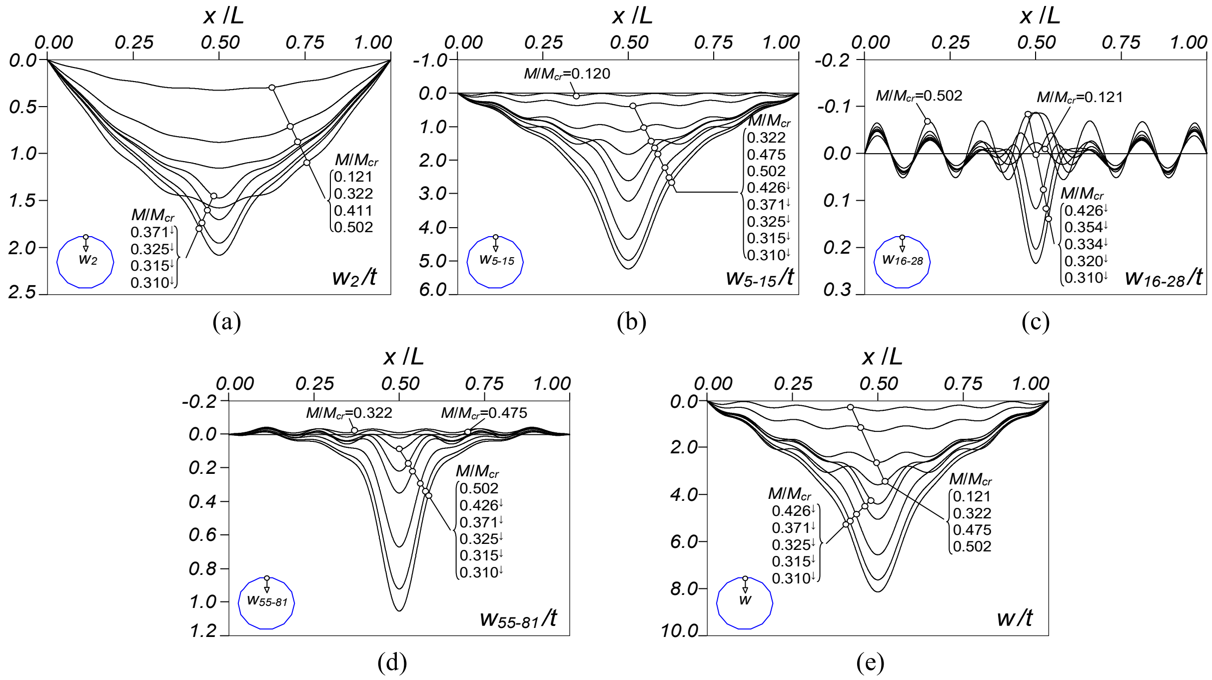

(a) (b) (c)

(d) (e)

Figure 18: Longitudinal displacement profiles of the RCPS (n=14, β_2=20, t=5.0mm, L=6r) beam with the –0.5mm initial imperfection: (a) $w_2(x)$, (b) $w_{5\text{-}15}(x)$, (c) $w_{16\text{-}28}(x)$, (d) $w_{55\text{-}81}(x)$, and (e) $w_{1\text{-}108}(x) \equiv w(x)$.

(v) The post-buckling behavior of n=20+β_2=20 beams with w_0>0 (Fig. 13(b_1)) only differs in the early-to-moderate post-buckling stages. In these beams, the 5 half-wave amplitudes increase gradually along the equilibrium path first ascending and descending branches. Then, along the second ascending branches the outer half-wave amplitudes become much smaller than the inner ones and the beam central regions become practically "flat" (see configuration "B" in Fig. 13(b_1)). From here on (second descending branches), a localized "kink" begins to develop at the mid-span region and the post-buckling behavior becomes similar to that described in item (iv). The structural responses of the 6 beams (Figs. 13(b_1)+(b_2)) become practically identical for $(w+w_0)/t$>2.5 (coincident equilibrium paths) – *e.g.*, compare, the configurations "C" in Figs. 13(b_1) and 13(b_2). While the behavior of the n=14+β_2=20 beam with w_0=+0.5mm (Fig. 13(a_1)) is qualitatively similar to those just addressed, the beams with w_0=+0.1 and w_0=+0.2mm behave differently: the initial 7 half-waves gradually change to 3 half-waves (see, configuration "C" in Fig. 13(a_1)). On the other hand, all the non-trivial paths displayed in Figs. 13(a_1)+(b_1) exhibit non-symmetric deformations, as attested by the deformed configurations "D" and "E" shown in those figures. A detailed discussion of this behavioral feature is addressed at the end of the section, for longer beams.

(vi) Like Fig. 13(a_1), Fig. 14(a_1) shows that the n=14+β_2=20 beam with L=6r also exhibits one alternative equilibrium path when the critical-mode initial geometrical imperfection has an odd half-wave number and involves mid-span outward motions. The remaining beams (Figs. 14(a_2)+(b)) do not exhibit alternative (non-trivial) solutions.

(vii) The comparison between Figs. 13(a_1)+(a_2) and Figs. 14(a_1)+(a_2) shows that both beam sets are imperfection-dependent, *i.e.*, a w_0 variation influences significantly the maximum moment reached. For the longer beams, however, the differences between the maximum moments decrease and the beam stiffness is more rapidly eroded due to the Brazier effect, which outweighs the influence of the initial geometrical imperfection amplitude.

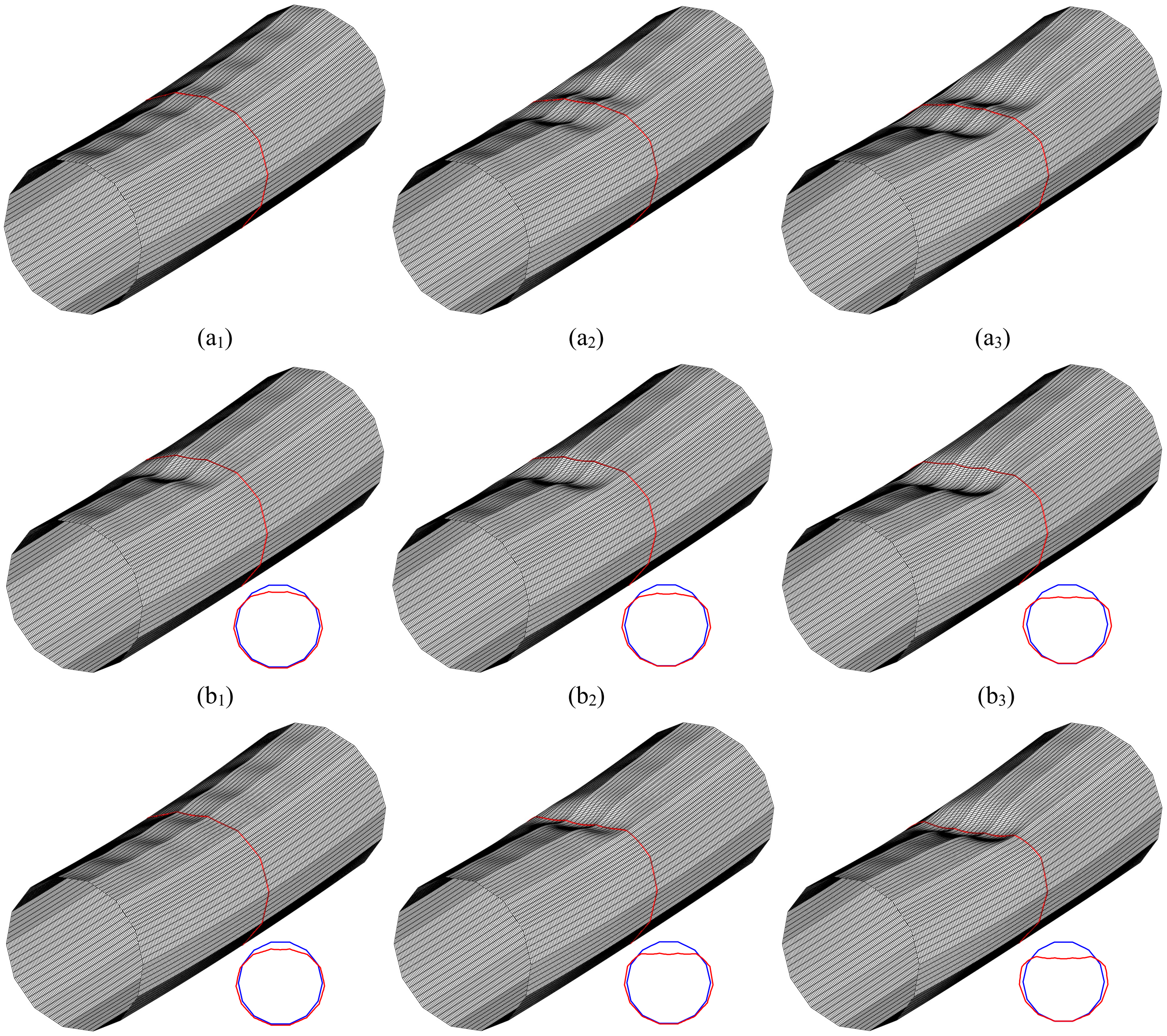
(a$_1$) (a$_2$) (a$_3$)

(b$_1$) (b$_2$) (b$_3$)

(c$_1$) (c$_2$) (c$_3$)

Figure 19: GBT-based deformed configurations of beams 10 (n=14, β_2=20 and L=6r) with (a) +0.5mm (trivial path), (b) +0.5mm (non-trivial path) and (c) −0.5mm initial imperfections at equilibrium states “A”, “B”, “C”, “D”, “E”, “F” in Figs. 14(a$_1$)+(a$_2$).

(viii)Figs. 15(a$_1$)+(b) show qualitatively similar modal participation evolutions. As expected, the major-axis flexural mode is always dominant, especially in the early loading stages. However, its relevance is rapidly reduced (in relative terms) along the trivial equilibrium path: it is gradually replaced mainly by the distortional mode contribution (mostly modes **5**+**6**+**8**+**7** – ordered in descending importance). Indeed, $p_{5\text{-}15}$ increases from 2.1% (first equilibrium point determined) (viii$_1$) to 55.6% at $(w+w_0)/t≅6.0$ in Fig. 15(a$_1$) (p_5=25.5%, p_6=14.1%, p_8=8.6%, p_7=3.9%) and (viii$_2$) to 55.1% at $(w+w_0)/t≅8.0$ in Fig. 15(b) (p_5=25.5%, p_6=14.2%, p_8=7.9%, p_7=3.6%). The joint contribution of the shear and linear transverse extension modes remains more or less constant up to the elastic limit point and increases slowly along the equilibrium path descending branch, reaching (viii$_1$) $p_{29\text{-}54}$=10.6% (p_{29}=4.7%, p_{31}=1.9%, p_{32}=1.1%) and $p_{55\text{-}81}$=8.42% (p_{67}=1.7%, p_{65}=0.8%, p_{55}=0.7%) at $(w+w_0)/t≅6.0$ in Fig. 15(a$_1$), and (viii$_2$) $p_{29\text{-}54}$=9.8% (p_{29}=4.4%, p_{31}=1.8%, p_{32}=1.0%) and $p_{55\text{-}81}$=7.9% (p_{67}=1.6%, p_{65}=0.8%, p_{55}=0.6%) at $(w+w_0)/t≅8.0$ in Fig. 15(b). The comparison between Figs. 15(a$_1$) and 15(a$_2$) shows differences in the participations of the major-axis flexural and distortional modes. While the latter remains almost constant (varies between 49.5% and 54.1%, with mode **7** now more relevant than mode **8**), the former decreases from 37.5% to 21.1% and, thus, the contribution of the shear and transverse extension modes increases. It is still worth noting that the local modal contribution is negligible in all the beams analyzed (it never exceeds 1.2%).

(ix) The analysis of the longitudinal profiles shown in Figs. 16(a)-(e) (w_0= +0.50mm) and Figs. 18(a)-(e) (w_0= –0.50mm) reveals quite distinct structural responses, although both beams reach their limit points at virtually identical applied bending moments. The modal participation diagrams displayed in Figs. 15(a$_1$)+(b) show that the larger contributions to $w(x)$ stem from the major-axis flexural and distortional modes, and remain qualitatively similar along the respective equilibrium paths – their amplitudes increase up to the elastic limit point (see Figs. 16(a)+(b) and 18(a)+(b) for M/M_{cr}≤0.504 and M/M_{cr}≤0.502, respectively. While the former set of profiles exhibits a single "wavy" half-wave, the latter displays 13 half-waves, akin to the initial geometrical imperfection at the early loading stages (see Figs. 5(a$_7$)+(b$_7$)), that exhibit gradually more unequal amplitudes (the larger one occurs at mid-span), but all involving inward motions). Immediately after the limit point is reached, one (Fig. 18(e)) or three (Fig. 16(e)) "kink(s)" develop at the mid-span region, *i.e.*, the beam deformation becomes more localized at that region (*e.g.*, see the profiles at M/M_{cr}=0.320$^{\downarrow}$ or M/M_{cr}=0.310$^{\downarrow}$ in Figs. 16(e) and 18(e), respectively) – the adjacent half-wave amplitudes are significantly reduced along the descending branch. In fact, the number and pattern of the kinks occurring in the descending branch strongly depend on the initial geometrical imperfection shape (number of half-waves and their relative amplitudes in the mid-span region). Along the equilibrium path descending branch it is also noticeable the growing contribution of the transverse extension modes (Figs. 16(d) and 18(d)) and the resemblance of their longitudinal profiles with the distortional mode ones (Figs. 16(b) and 18(b)). The 3D deformed configurations displayed in Figs. 19(a$_1$)-(a$_3$) and 19(c$_1$)-(c$_3$), together with the corresponding 2D mid-span configurations (configurations "A", "B", and "C" on the equilibrium paths of Fig. 14(a$_1$)+(a$_2$)), also show/reinforce the difference between the post-buckling behaviors of these two beams. It is worth noting the qualitative similarity between the post-buckling behaviors of the L=3r (Fig. 13(a)) and L=6r (Fig. 14(a)) n=14+β_2=20 beams.

(x) The comparison between the longitudinal displacement profiles and deformed configurations of the trivial and non-trivial equilibrium paths (Figs. 16(a)-(e) vs. Figs. 17(a)-(e) and Figs. 19(a$_1$)-(a$_3$) vs. Figs. 19(b$_1$)-(b$_3$)) reveals dissimilar post-buckling behaviors. Indeed, immediately after the bifurcation point (beginning of the non-trivial path) one kink develops near the mid-span region (x/L≅0.58), leading to a deformed configuration change and the reduction of the $w_2(x)$ amplitude – see the dashed curves in Fig. 17(a) between M/M_{cr}=0.504 and M/M_{cr}=0.380$^{\downarrow}$. The latter equilibrium state is already associated with a pronounced beam deformation slightly "shifted" towards x/L>0.50 – this feature is shared by all the remaining modal contributions displayed in Figs. 17(b)-(d). The beam deformed configuration exhibits longitudinally asymmetry, unlike the beams discussed in the previous item – Figs. 19(b$_1$)-(b$_3$), concerning the configurations "D", "E" and "F" identified in Fig. 14(a$_1$), show this asymmetry very clearly – it is most likely due to the fact that this beam exhibits very close first two bifurcation moments, associated with consecutive half-wave numbers, as pointed out in Section 2.3. Indeed, the post-buckling behavior of this beam is qualitatively very similar to that displayed in Fig. 14(b) – beams containing initial geometrical imperfections with even half-wave numbers. Since the post-buckling behavior of this beam is also very similar to those discussed next, concerning n=20 and n=30 beams, its presentation and discussion is omitted from this work.

The next set of results is similar to those presented previously but concerns RCPS beams with n=20+β_2=20 (beam 15 of Table 1) and n=30+β_2=20 (beam 16 of Table 1). The GNIA results were obtained for critical-mode initial geometrical imperfections with 24 half-waves (see Figs. 5(a_8)+(a_9)), *i.e.*, with an even half-wave number. Figs. 20(a), 21(a) and 23(a) (beam 15), and Figs. 20(b), 21(b) and 23(b) (beam 16) show the (i) fundamental equilibrium paths M/M_{cr} vs. $(w+w_0)/t$, (ii) modal participation diagrams p_k vs. M/M_{cr} and (iii) deformed configurations at equilibrium states "A", "B" and "C", lying on the equilibrium paths in Figs. 20(a)-(b). Lastly, Figs. 22(a)-(e) show the contributions to the top wall mid-point transverse displacement profile $w(x)$ of the major-axis flexural, distortional, local and linear transverse extension modes, concerning the n=20+β_2=20 beam with w_0=0.50mm. The observation of these GNIA results leads to the following comments:

(i) There is a strong resemblance between the post-buckling behaviors of the n=20 and n=30 RCPS beams, as attested by the similar equilibrium paths, modal participation diagrams and deformed configurations. Therefore, the n=30 beam displacement profiles were not included in this paper.

(ii) As also observed in the n=14+β_2=20 beams (see Fig. 14(b) – initial geometrical imperfections with an even half-wave number), there are no alternative solutions in the equilibrium paths shown in Figs.

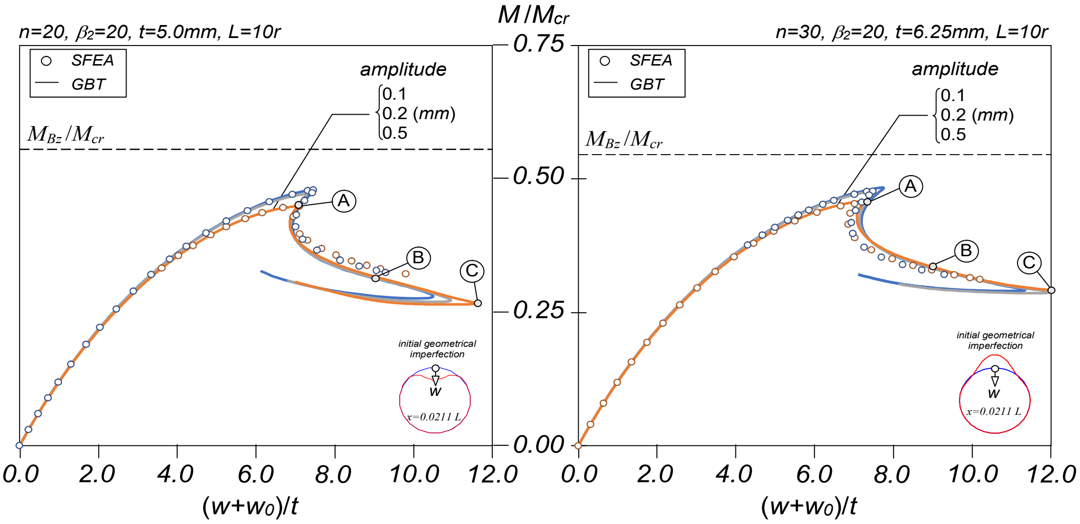

(a) (b)

Figure 20: Post-buckling equilibrium paths M/M_{cr} vs. $(w+w_0)/t$ of beams with critical-mode initial geometrical imperfections having several amplitudes: (a) n=20, β_2=20, t=5.0mm, L=10r, and (b) n=30, β_2=20, t=6.25mm, L=10r.

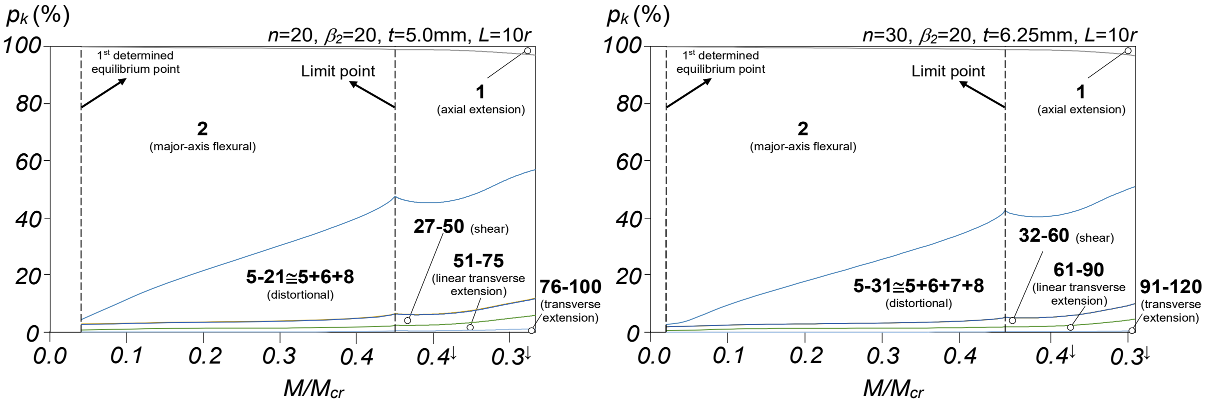

(a) (b)

Figure 21: Modal participation diagrams p_k vs. M/M_{cr} of (a) beam 15 (n=20, β_2=20, t=5.0mm, L=10r) and (b) beam 16 (n=30, β_2=20, t=6.25mm, L=10r).

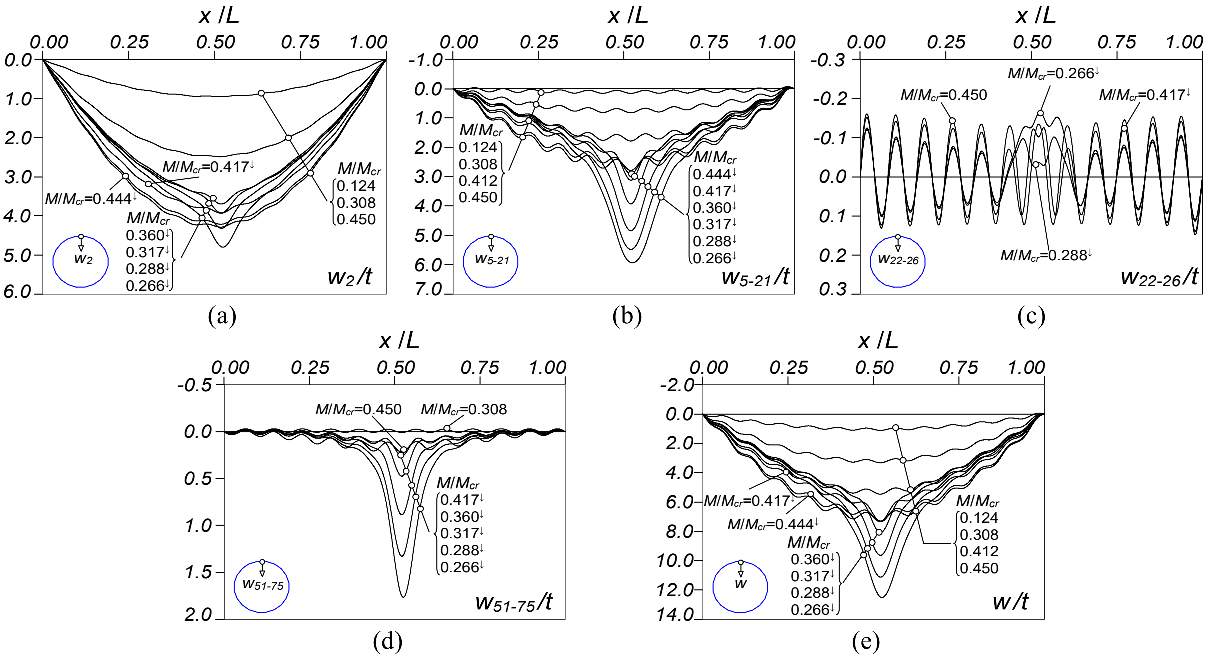

(a) (b) (c)

(d) (e)

Figure 22: Longitudinal displacement profiles of the RCPS (n=20, β_2=20, t=5.0mm, L=10r) beam with the 0.5mm initial imperfection: (a) $w_2(x)$, (b) $w_{5\text{-}21}(x)$, (c) $w_{22\text{-}26}(x)$, (d) $w_{51\text{-}75}(x)$, and (e) $w_{1\text{-}100}(x) \equiv w(x)$.

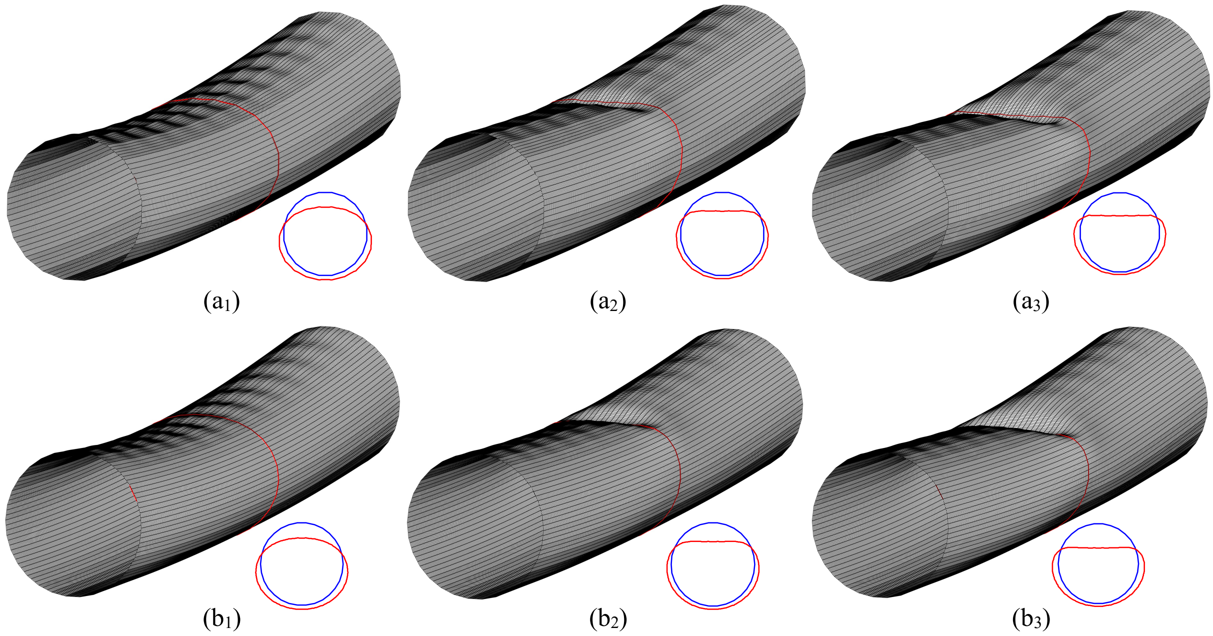

(a$_1$) (a$_2$) (a$_3$)

(b$_1$) (b$_2$) (b$_3$)

Figure 23: GBT-based deformed configurations of beams (a) 15 (n=20+β_2=20) and (b) 16 (n=30+β_2=20) at M/M_{cr} equal to (a$_1$) 0.450, (a$_2$) 0.317$^{\downarrow}$ and (a$_3$) 0.266$^{\downarrow}$ or (b$_1$) 0.459, (b$_2$) 0.335$^{\downarrow}$ and (b$_3$) 0.291$^{\downarrow}$ (equilibrium states "A", "B", "C" in Figs. 20(a)-(b)).

20(a)-(b) – the eigenvalue analysis of their GBT global tangent stiffness matrices did not reveal any new negative eigenvalue along the descending branches paths (up to $(w+w_0)/t$=12.0, at least).

(iii) The comparison between the equilibrium paths displayed in Figs. 14(b) and 20(a)-(b) shows that the stiffness of the latter beams is more rapidly eroded along the equilibrium path ascending branches (the limit point is reached "sooner"), due to the fact that they are significantly longer (10r vs. 6r).

Moreover, the limit point is also considerably below the Brazier moment: M_{Bz}/M_{cr}=0.585, for n=14+β_2=20, M_{Bz}/M_{cr}=0.556, for n=20+β_2=20, and M_{Bz}/M_{cr}=0.546, for n=30+β_2=20.

(iv) The displacement profiles displayed in Figs. 22(a)-(e) show, along the n=20+β_2=20 RCPS beam equilibrium path ascending branch, major contributions from major-axis bending (mode **2**) and the distortional modes (modes **5-21**), as quantified in Fig. 21(a). The former exhibits an almost sinusoidal shape (see Fig. 22(a)) and the latter displays initially 24 half-waves (see Fig. 5(a_8) or Fig. 22(b) for M/M_{cr}=0.124) that then combine with a gradually growing sinusoid (see Fig. 22(b) for M/M_{cr}=0.412). Beyond the limit point, the post-buckling behavior is similar to that exhibited by the non-trivial equilibrium path in Fig. 14(a_1) (n=14+β_2=20 RCPS beam). Indeed, a localized "kink" develops near mid-span (region adjacent to the half-wave with inward motions – $x/L\cong0.52$). It grows considerably along the equilibrium path descending branch, as visible in the deformed configurations "B" and "C" in Figs. 23(a_2)+(a_3). The n=14 and n=20 RCPS beams only differ in the location of the "kink" – closer to mid-span in the latter beam, due to the larger number of initial imperfection half-waves.

Given the findings of this section, it is concluded that all beams analyzed exhibit a *shell-like* behavior: unstable equilibrium paths, imperfection sensitivity, possible occurrence of bifurcated equilibrium paths and inability to sustain applied moments similar to the Brazier moment. The elastic failure moment is always well below the critical buckling moment, particularly for high length-to-circumradius ratios.

3.3 Local-distortional interactive post-buckling behavior

This last section deals with the beams selected in Section 2.3 that buckle in mixed local-distortional modes, namely RCPS beams (i) with n=10 and β_2=20,35,50,65 (beams 5-8 in Table 1), and (ii) with n=14 and β_2=20,40,60,100 (beams 10-13 in Table 1)[16]. Figs. 24(a)-(d) and 25(a)-(d) show the equilibrium paths M/M_{cr} vs. $(w+w_0)/t$ of these beams, which have critical-mode initial geometrical imperfections with an even half-wave number and several amplitudes (w is again the mid-span flexural displacement at the top wall mid-point). Figs. 26(a_1)-(b_3) display beam deformed configurations at the equilibrium states identified on the equilibrium paths in Figs. 24(a) and 25(b). As in the previous section, all existing non-trivial equilibrium paths were determined and are also displayed in Figs. 24(a)-(d) and 25(a)-(d). After examining the equilibrium paths depicted in these figures, it is worth noting that:

(i) As β_2 increases, the post-buckling behaviors exhibited by both the n=10 and n=14 RCPS beams change remarkably. Indeed, a pronounced decrease in the stiffness erosion is observed, which corresponds to a gradual transition from a highly unstable post-buckling behavior to less unstable ones and, ultimately (for a sufficiently large β_2 value), to a stable post-buckling behavior. This change in equilibrium path nature is accompanied by increasing M_{Bz}/M_{cr} values.

(ii) The post-buckling behaviors of the n=10+β_2=65 (Fig. 24(d)) and n=14+β_2=100 (Fig. 25(d)) beams are qualitatively similar to the local post-buckling behavior addressed and characterized in Section 3.1, in the context of RCPS beam with lower n values – indeed, they exhibit highly stable post-critical behaviors. Their elastic limit points only occur for much higher applied moments (not shown in the figures) and are triggered by the Brazier effect. Moreover, no non-trivial equilibrium paths were detected in these beams.

(iii) Conversely, the post-buckling behaviors of the n=10+β_2=20 (Fig. 24(a)) and n=14+β_2=20 (Fig. 25(a)), which are quite close[17], are qualitatively similar to the distortional post-buckling behavior

---

[16] Note that the beam with n=14 and β_2=20 shown in Fig. 25(a) is identical to that whose equilibrium paths are displayed in Fig. 14(b).

[17] Although the stiffness of the n=10+β_2=20 RCPS beam (fundamental) equilibrium paths are "more rapidly eroded", it should be noted that the length considered is a bit higher (L=7r vs. L=6r).

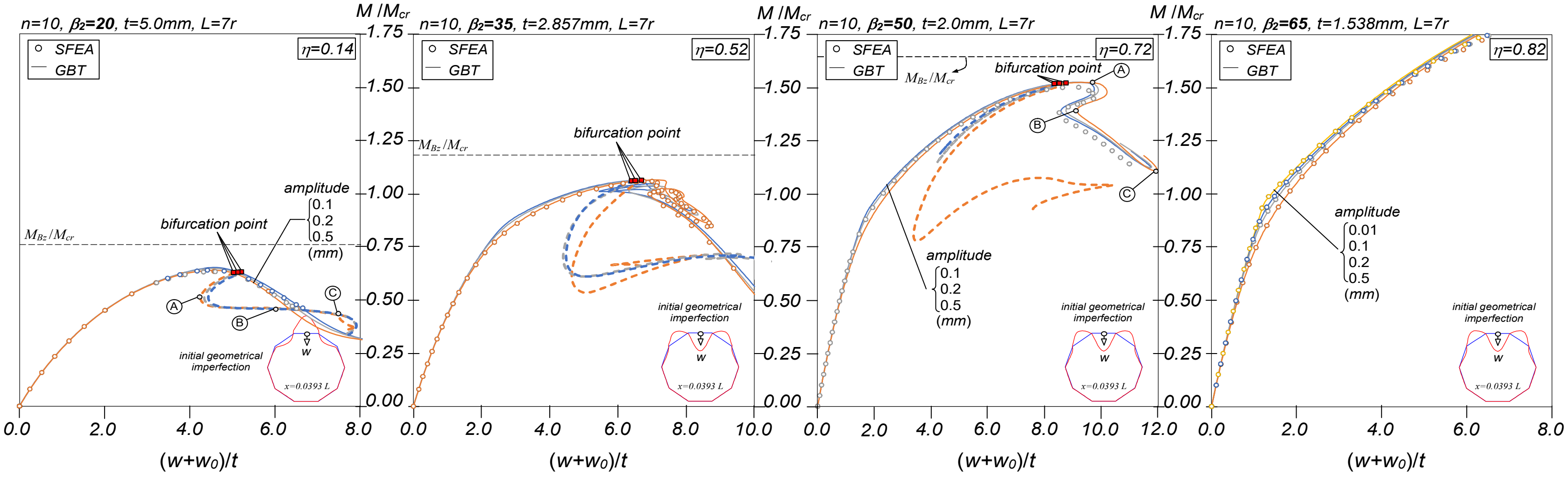

(a) (b) (c) (d)

Figure 24: Post-buckling equilibrium paths M/M_{cr} vs. $(w+w_0)/t$ of RCPS beams (n=10, r=100mm, L=7r) with critical-mode initial geometrical imperfections having several amplitudes: (a) β_2=20, (b) β_2=35, (c) β_2=50 and (d) β_2=65.

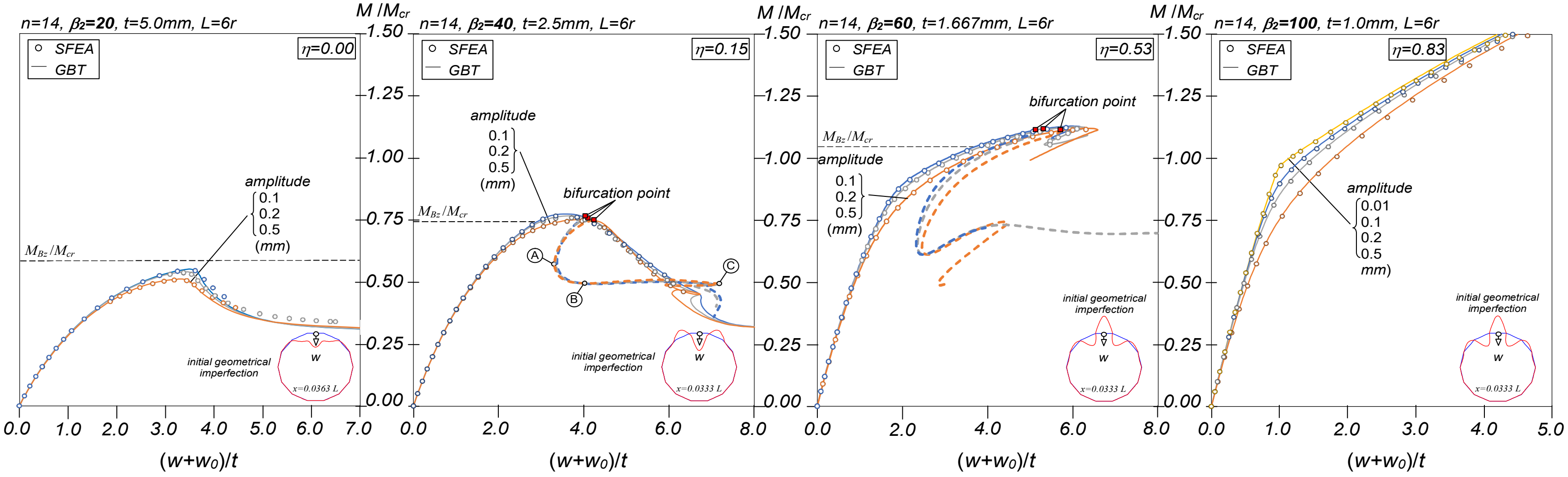

(a) (b) (c) (d)

Figure 25: Post-buckling equilibrium paths M/M_{cr} vs. $(w+w_0)/t$ of RCPS beams (n=14, r=100mm, L=6r) with critical-mode initial geometrical imperfections having several amplitudes: (a) β_2=20, (b) β_2=40, (c) β_2=60 and (d) β_2=100.

addressed and characterized in Section 3.2. The sole difference between them is the fact that the former beams exhibit one non-trivial equilibrium path, emerging in the beginning of the fundamental path descending branch (immediate vicinity of the limit point). The quite surprising behavior associated with this non-trivial equilibrium path is illustrated by the 3D and 2D mid-span beam deformed configurations "A", "B", "C" displayed in Figs. 26(a_1)-(a_3) for the n=10+β_2=20 beam with the 0.5mm initial imperfection. These deformed configurations show that this beam does not remain symmetric with respect to the (vertical) axis normal to the bending one. Indeed, they are symmetric with respect to an axis passing through one corner of the most compressed wall (the left one, in Figs. 26(a_1)-(a_3)), unlike their fundamental equilibrium path counterparts, which retain the vertical symmetry. This feature was never observed in the beams analyzed in Section 3.2.

(iv) The beam equilibrium paths displayed in Figs. 24(a)-(d) and 25(a)-(d) show that the post-buckling behaviors of the n=10+β_2=35, n=10+β_2=50, n=14+β_2=40 and n=14+β_2=60 RCPS beams combine features of the local and distortional post-buckling behaviors, *i.e.*, they undergo local-distortional interaction. In addition, it is also noticeable that the post-buckling behaviors of the n=10+β_2=35 and n=14+β_2=40 beams are closer to distortional, while those of the n=10+β_2=50 and n=14+β_2=60 beams are closer to local. For a given η value, the n=14 RCPS beams exhibit slightly larger failure moments – *e.g.*, compare the failure moment ratios M_{max}/M_{cr} in (iv_1) Figs. 24(a) and 25(b) (0.65 vs. 0.77 – η=0.14 and η=0.15) and (iv_2) Figs. 24(b) and 25(c) (1.07 vs. 1.12 – η=0.52 and η=0.53).

(v) Denoting by η_{ref} the values of η corresponding to the solid curve shown in Fig. 2(b), it is possible to conclude that the beams either do not exhibit post-critical strength, if $\eta<\eta_{ref}$, or exhibit a significant post-critical strength, if $\eta>\eta_{ref}$. For instance, for n=10 one has η_{ref}=0.46 and Figs. 24(a)-(d) show that the η=0.14 beams (Fig. 24(a)) do exhibit post-critical strength, unlike the remaining beams (Figs.

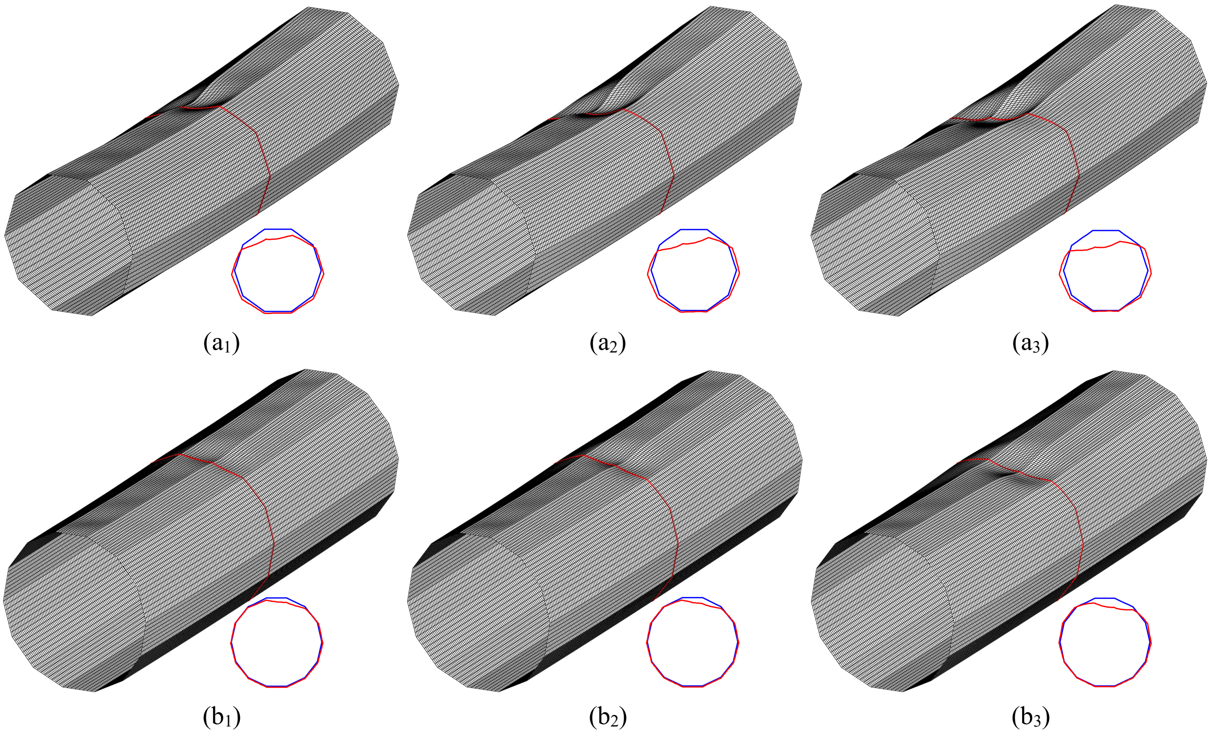
(a_1) (a_2) (a_3)

(b_1) (b_2) (b_3)

Figure 26: GBT-based deformed configurations of beams (a) 5 (n=10+β_2=20) and (b) 11 (n=14+β_2=40) at equilibrium states "A", "B", "C" identified in Figs. 24(a) and 25(b).

24(b)-(d)), for which η is equal to 0.52, 0.72 and 0.82, respectively. Similar conclusions can be drawn for the n=14 beams whose equilibrium paths are shown in Figs. 25(a)-(d).

(vi) Lastly, the characteristics of all the non-trivial equilibrium paths displayed in Figs. 24(b)+(c) and 25(b)+(c) are similar to those presented and discussed in item (iii) – in particular, the beam deformed configurations exhibit symmetry with respect to a rotated axis. Figs. 26(b_1)-(b_3) show deformed configurations of the n=14+β_2=40 beam with a 0.5mm critical-mode initial imperfection along its non-trivial path equilibrium path.

4. Concluding Remarks

This paper presented and discussed the results of a numerical investigation on the elastic post-buckling behavior of simply supported regular convex polygonal cross-section (RCPS) tubes subjected to uniform bending and buckling in local, distortional or mixed local-distortional modes. These results were obtained through GBT-based geometrically non-linear analyses enriched with a branch switching technique and validated by the comparison with values yielded by ABAQUS shell finite element models, when possible[18]. After addressing and characterizing the buckling (bifurcation) behavior of RCPS beams, on the basis of their wall numbers (n) and circumradius-to-thickness ratios (β_2), relevant beam geometries were selected and attention was turned to studying their elastic post-buckling behaviors. Particular attention was paid to the imperfection sensitivity and the mechanics underlying three distinct types of post-buckling behavior. Out of the various findings obtained in this investigation, the following deserve to be specially highlighted:

(i) Depending on the β_2 value, any RCPS beam with n walls may buckle in local, distortional or mixed local-distortional modes. Distortional buckling invariably occurs for low β_2 values and, as β_2 grows, the beam gradually becomes susceptible to mixed local-distortional buckling until a buckling coefficient plateau is reached, which corresponds to local buckling. However, the β_2 value associated with the transition from mixed local-distortional to local buckling increases considerably with n.

(ii) As already done by Gonçalves & Camotim (2013b), it was confirmed that the classical formula for axisymmetric buckling of uniformly compressed circular tubes (Timoshenko & Gere 1961) provides excellent estimates for the distortional buckling coefficient for RCPS beams under uniform bending.

(iii) It was shown that the transition between local and distortional buckling is rather steep and that the degree of displacement-restraint at the wall ends/corners strongly impacts the post-buckling behavior and strength of such beams (see item (ix) below).

(iv) Since pure local elastic post-buckling behavior of RCPS beams is highly stable (like its column counterpart – Martins *et al.* 2019a), they are able to sustain applied moments considerably higher than their critical buckling moments (*plate-like* behavior) – the elastic limit point, invariably caused by the Brazier effect, occurs well above the critical buckling moment. Moreover, no imperfection sensitivity was observed (only critical-mode initial geometrical imperfections were considered).

(v) The RCPS beam pure distortional elastic post-buckling behavior of RCPS beams is highly unstable and imperfection sensitive. In general, like in cylindrical tubes, this post-buckling behavior is characterized by equilibrium paths exhibiting initial small linear regions, followed by pronounced non-linear branches reflecting a more or less rapid stiffness erosion, due to cross-section ovalisation (Brazier effect), and leading invariably to elastic limit points, occurring well below the critical buckling moment (*shell-like* behavior). Then, depending on the initial geometrical imperfection shape, more or less smooth equilibrium path descending branches follow.

---

[18] Only fundamental/trivial equilibrium paths could be obtained by means of ABAQUS SFEA.

(vi) In beams buckling in distortional modes, the consideration of specific initial geometrical imperfection shapes, such as those involving odd half-wave number with outward mid-span motions, invariably led to a loss of uniqueness of the numerical solution immediately after the elastic limit point is reached (in the beginning of the equilibrium path descending branch). Since only one new negative eigenvalue of the global tangent stiffness matrix was detected along the equilibrium path descending branch, these beams exhibit one trivial/fundamental and one non-trivial/alternative equilibrium paths (the latter branches out of the bifurcation point – see item (vii) below). Regardless of the initial geometrical imperfection shape, the beam response always leads to the development of (at least) one localized "kink", not necessarily at mid-span, that grows considerably along the descending branch (trivial or non-trivial). Note that RCPS columns buckling in distortional modes (Martins *et al.* 2019a) also have unstable equilibrium paths. However, unlike the RCPS beams analyzed in this work, the columns always exhibit non-trivial equilibrium paths emerging from bifurcation points located on the fundamental equilibrium path descending branch (regardless of the initial geometrical imperfection shape and amplitude).

(vii) The structural response associated with the non-trivial equilibrium paths mentioned in item (vi) strongly resembles between that of a beam with the same geometry and an initial geometrical imperfection with an odd half-wave number. This similarity is most likely due to fact that the two lowest bifurcation moments are very close and correspond to buckling modes with consecutive half-wave numbers (one odd and the other even).

(viii)The beam length influences considerably the elastic failure moment, which is gradually smaller as the length increases, regardless of the post-buckling behavior nature (local, distortional or local-distortional interactive). In addition, the elastic failure moments fall gradually below the Brazier moment as a given beam length increases.

(ix) The post-buckling behaviors of all the RCPS beams undergoing local-distortional interaction analyzed in this work were shown strongly dependent on the η value (degree of displacement restraint at the wall ends/corners). Indeed, there is a remarkably post-critical strength increase as η grows, corresponding to a gradual transition between pure distortional (unstable) and pure local (highly stable) post-buckling behaviors. Non-trivial equilibrium paths were detected in all the beams experiencing local-distortional interaction (emerging in the vicinity of the elastic limit point – either immediately before or after this point). Along these equilibrium paths, the beam deformed configuration exhibited symmetry with respect to a rotated axis (not the axis normal to the bending one) – note that only initial geometrical imperfections with even half-wave numbers were considered. These features contrast with those observed in beams exhibiting pure distortional post-buckling behaviors, for which (ix_1) no non-trivial equilibrium path was detected when the initial geometrical imperfections had even half-wave numbers and (ix_2) the non-trivial equilibrium paths always emerged from bifurcation points located after the limit point.

Finally, one last word to mention that work is currently under way to assess the elastic-plastic behavior and strength of RCPS beams, an indispensable step in the path towards developing rational and efficient design rules for such members (the ultimate goal of the ongoing research effort). In this regard, it is worth noting that, to the authors' best knowledge, the only existing European standard that addresses RCPS members is the EN 40-3-3 (CEN 2013), even if only octagonal and cylindrical tubes are considered – naturally, a careful examination of the performance of these existing design rules is also planned. But it is clear that reliable design rules for RCPS members must account for the strength variation reflected by the β_2 value.

References

Bebiano, R., Gonçalves, R., Camotim, D. (2015). "A cross-section analysis procedure to rationalize and automate the performance of GBT-based structural analysis". *Thin-Walled Structures*, 92(July), 29-47.

Bebiano, R., Camotim, D., Gonçalves, R. (2018). "GBTUL 2.0 – a second-generation code for the GBT-based buckling and vibration of thin-walled members", *Thin-Walled Structures*, 124(March), 235-257.

Bernard, E.S., Bridge, R.Q., Hancock, G.J. (1996). "Flange curling in profiled steel decks", *Thin-Walled Structures*, 25(1), 1-29.

Borst, R., Crisfield, M.A., Remmers, J.J.C., Verhoosel, C.V. (2012). *Non-linear Finite Element Analysis of Solids and Structures* (2nd edition), John Wiley & Sons Ltd (Chichester).

Brazier, L.G. (1927). "On the flexure of thin cylindrical shells and other "thin" sections", *Proceedings of the Royal Society A: Mathematical, Physical and Engineering Sciences*, 116(773), 104-114.

Bulson, P.S. (1969). "The strength of thin-walled tubes formed from flat elements", *International Journal of Mechanical Sciences*, 11(July), 613-620.

Camotim, D., Basaglia, C., Bebiano, R., Gonçalves, R., Silvestre, N. (2010a). "Latest developments in the GBT analysis of thin-walled steel structures", *Proceedings of International Colloquium on Stability and Ductility of Steel Structures* (SDSS'Rio 2010 – Rio de Janeiro, 8-10/9), E. Batista, P. Vellasco, L. Lima (eds.), 33-58 (Vol. 1).

Camotim, D., Basaglia, C., Silva, N.F., Silvestre, N. (2010b). "Numerical analysis of thin-walled structures using Generalised Beam Theory (GBT): recent and future developments", *Computational Technology Reviews*, vol. 1, B. Topping *et al.* (eds.), Saxe-Coburg (Stirlingshire), 315-354.

Camotim, D., Basaglia, C. (2013). "Buckling analysis of thin-walled structures using Generalised Beam Theory (GBT): state-of-the-art report", *Steel Construction*, 6(2), 117-131.

CEN (Comité Européen for Standardization) (2013). EN 40-3-3, *Lighting Columns – Part 3-3: Design and Verification – Verification by Calculation*, Brussels.

Gonçalves, R., Camotim, D. (2011). "Generalised beam theory-based finite elements for elastoplastic thin-walled metal members", *Thin-Walled Structures*, 49(10), 1327-1245.

Gonçalves, R., Camotim, D. (2012). "Geometrically non-linear Generalised Beam Theory for elastoplastic thin-walled metal members", *Thin-Walled Structures*, 51(February), 121-129.

Gonçalves, R., Camotim, D. (2013a). "Elastic buckling of uniformly compressed thin-walled regular polygonal tubes", *Thin-Walled Structures*, 71(October), 35-45.

Gonçalves, R., Camotim, D. (2013b). "Buckling behaviour of thin-walled regular polygonal tubes subjected to bending or torsion", *Thin-Walled Structures*, 73(December), 185-197.

Gonçalves, R., Camotim, D. (2013c). "On the behaviour of thin-walled steel regular polygonal tubular members", *Thin-Walled Structures*, 62(January), 191-205, 2013.

Gonçalves, R., Bebiano, R., Camotim, D. (2014). "On the shear deformation modes in the framework of Generalized Beam Theory", *Thin-Walled Structures*, 84(November), 325-334.

Ju, G.T., Kyriakides, S. (1992). "Bifurcation and localization instabilities in cylindrical shells under bending – II. predictions", *International Journal of Solids and Structures*, 29(9), 1143-1171.

Kim, S.J., Shin, J.W., Kim, H.-G., Kim, T.-U., Kim, S. (2016). "The modified Brazier approach to predict the collapse load of a stiffened circular composite spar under bending load", *Aerospace Science and Technology*, 55(August), 474-481.

Kyriakides, S., Ju, G.T. (1992). "Bifurcation and localization instabilities in cylindrical shells under bending – I. experiments", *International Journal of Solids and Structures*, 29(9), 1117-1142.

Lecce, M., Rasmussen, K.J.R. (2008). "Nonlinear flange curling in wide flange sections", *Journal of Constructional Steel Research*, 64(7-8), 779-784.

Martins, A.D., Camotim, D., Gonçalves, R., Dinis, P.B. (2018a). "On the mechanics of local-distortional interaction in thin-walled lipped channel beams", *Thin-Walled Structures*, 128(July), 108-125.

Martins, A.D., Camotim, D., Gonçalves, R., Dinis, P.B. (2018b). "Enhanced geometrically non-linear Generalized Beam Theory (GBT) formulation: derivation, numerical Implementation and illustration", *Journal of Engineering Mechanics* (ASCE), 144(6), paper 04018036 (20 pages).

Martins, A.D., Camotim, D., Gonçalves, R., Dinis, P.B. (2018c). "On the mechanics of distortional-global interaction in fixed-ended columns", *Thin-Walled Structures*, 123(February), 162-184.

Martins, A.D., Gonçalves, R., Camotim, D. (2019a). "On the local and distortional post-buckling behaviour of thin-walled regular polygonal tubular columns", *Thin-Walled Structures*, 138(May), 46-63.

Martins, A.D., Gonçalves, R., Camotim, D. (2019b). "Post-buckling behaviour of thin-walled regular polygonal tubular columns undergoing local-distortional interaction", *Thin-Walled Structures*, 138(May), 373-391.

Reissner, E. (1961). "On finite pure bending of cylindrical tubes", *Österreichisches Ingenieur – Archive*, 15(1-4), 165-172.

Reissner, E., Weinitschke, H.J. (1963). "Finite pure bending of circular cylindrical tubes", *Quarterly of Applied Mathematics*, 20(4), 305-319.

Sanders, J.L. (1963). "Nonlinear theories of thin shells", *Quarterly of Applied Mathematics*, 21(1), 21-36.

Schardt, R. (1989). *Verallgemeinerte Technische Biegetheorie*, Berlin, Springer-Verlag. (German)

Simulia, Inc. (2009). ABAQUS Standard (version 6.9-3).

Silvestre, N. (2007). "Generalised beam theory to analyse the buckling behaviour of circular cylindrical shells and tubes", *Thin-Walled Structures*, 45(2), 185-198.

Tatting, B.F., Gürdal, Z., Vasiliev, V.V. (1997). "The Brazier effect for finite length composite cylinders under bending", *International Journal of Solids and Structures*, 34(12), 1419-1440.

Timoshenko, S., Gere, J. (1961). *Theory of Elastic Stability*, New York, McGraw-Hill.

Wadee, M.K., Wadee, M.A., Bassom, A.P., Aigner, A.A. (2006). "Longitudinally inhomogeneous deformation patterns in isotropic tubes under pure bending", *Proceedings of the Royal Society A: Mathematical, Physical and Engineering Sciences*, 462(2067), 817-838.

Wierzbicki, T., Sinmao, M.V. (1997). "A simplified model of Brazier effect in plastic bending of cylindrical tubes", *International Journal of Pressure Vessels and Piping*, 71(1), 19-28.

Yadav, K.K., Gerasimidis, S. (2019). "Instability of thin steel cylindrical shells under bending", *Thin-Walled Structures*, 137(April), 151-166.